

Particle acceleration and magnetic dissipation in relativistic current sheet of pair plasmas

S. Zenitani

*NASA Goddard Space Flight Center, Greenbelt, MD 20771;
zenitani@lssp-mail.gsfc.nasa.gov*

M. Hoshino

*Department of Earth and Planetary Science, University of Tokyo, 7-3-1, Hongo, Bunkyo,
Tokyo, 113-0033 Japan*

ABSTRACT

We study linear and nonlinear development of relativistic and ultrarelativistic current sheets of pair (e^\pm) plasmas with antiparallel magnetic fields. Two types of two-dimensional problems are investigated by particle-in-cell simulations. First, we present the development of relativistic magnetic reconnection, whose outflow speed is on the order of the light speed c . It is demonstrated that particles are strongly accelerated in and around the reconnection region and that most of the magnetic energy is converted into a “nonthermal” part of plasma kinetic energy. Second, we present another two-dimensional problem of a current sheet in a cross-field plane. In this case, the relativistic drift kink instability (RDKI) occurs. Particle acceleration also takes place, but the RDKI quickly dissipates the magnetic energy into plasma heat. We discuss the mechanism of particle acceleration and the theory of the RDKI in detail. It is important that properties of these two processes are similar in the relativistic regime of $T \gtrsim mc^2$, as long as we consider the kinetics. Comparison of the two processes indicates that magnetic dissipation by the RDKI is a more favorable process in the relativistic current sheet. Therefore, the striped pulsar wind scenario should be reconsidered by the RDKI.

Subject headings: acceleration of particles — magnetic fields — plasmas — relativity — stars: winds, outflows — pulsars: individual (Crab Pulsar)

1. Introduction

Magnetic reconnection is an important large-scale process in space plasmas. By rearranging the magnetic field topology, it causes heating and particle acceleration of plasmas as

well as dissipation of the magnetic fields. Although it has been extensively studied in wide range of solar terrestrial sites— stellar and solar flares (Parker 1957), the planetary magnetospheres (Dungey 1961; Russell et al. 1998) and solar wind (Phan et al. 2006)— it has also been discussed in high-energy astrophysical contexts such as the magnetized loop of the Galactic center (Heyvaerts et al. 1988), the jets from active galactic nuclei (di Matteo 1998; Schopper et al. 1998; Lesch & Birk 1998; Larrabee et al. 2003), quite probably gamma-ray bursts (Drenkhahn & Spruit 2002), and pulsar winds (Michel 1982; Coroniti 1990; Michel 1994). In these situations, reconnection often takes place in relativistic electron-positron plasmas. Especially in the Crab pulsar wind, in the relativistic outflow of pair plasmas from the central neutron star, relativistic reconnection or relevant processes have been considered as possible processes to explain the long-standing “ σ -problem” (σ is the ratio of the Poynting flux energy to the particle kinetic flux); the plasma outflow is originally Poynting-dominated ($\sigma \sim 10^4$) close to the neutron star (Arons 1979), but it should be kinetic-dominated near the downstream termination shock ($\sigma \sim 10^{-3}$; Kennel & Coroniti (1984)). The possible dissipation mechanisms are instabilities in the striped current sheets; due to the fast rotation of the central neutron star, whose magnetic dipole is in the oblique direction, alternating magnetic fields are strongly “striped” near the equatorial plane. We assume that there are current sheets between such opposite magnetic field lines, and magnetic reconnection occurs and dissipates the magnetic energy there (Coroniti 1990). Based on this idea, magnetic dissipation in the pulsar wind has been estimated by using a one-dimensional MHD model (Lyubarsky & Kirk 2001; Kirk & Skjæraasen 2003), but they were not so successful. The main problem is that basic properties of relativistic reconnection or current sheet processes are still unclear.

Until recent years, there have been few theoretical studies on relativistic reconnection. Zelenyi & Krasnoselskikh (1979) studied the relativistic kinetic description of the tearing instability, which is the most important instability in the reconnection context. Blackman & Field (1994) studied the steady state reconnection models in relativistic pair plasmas. They argued that the reconnection rate becomes closer to the unity due to Lorentz effects, and therefore, faster energy conversion is possible. These steady models are further investigated by several authors (Lyutikov & Uzdensky 2003; Lyubarsky 2005), although there is controversy about whether inflow speed can be relativistic or not. On the viewpoint of particle acceleration, Romanova & Lovelace (1992) studied the particle orbits in the reconnection field model, and they obtained an energetic energy spectrum of pair plasma, which is approximated by the power-law distribution with an index of -1.5 . Larrabee et al. (2003) obtained the power-law index of -1 , assuming that particle motion is restricted in the neutral plane. In a fully self-consistent way, relativistic magnetic reconnection has recently been explored by particle-in-cell (PIC) simulations (Zenitani & Hoshino 2001, 2005b; Jaroschek et

al. 2004). Zenitani & Hoshino (2001) demonstrated that an enhanced dc acceleration takes place in and around the X -type region, due to the reconnection electric field E_y . This acceleration is so strong that a power law index of the energy spectrum around the acceleration site is on the order of -1 (Zenitani & Hoshino 2001), and the energy spectrum over the whole simulation domain is approximated by the power-law with an index of -3 (Jaroschek et al. 2004). Using relativistic resistive MHD code, Watanabe & Yokoyama (2006) presented Petschek reconnection in the mildly relativistic case.

The current sheet configuration with antiparallel magnetic field lines is also influenced by cross field instabilities, whose wavevectors are perpendicular to the reconnection plane. In geophysical contexts, the lower hybrid drift instability (LHDI) (Krall & Liewer 1971; Davidson et al. 1977) may be of importance, and it leads to transport of plasma heat (Huba & Drake 1981) and the fast triggering of magnetic reconnection (Shinohara & Fujimoto 2005; Tanaka et al. 2006). The Kelvin-Helmholtz instability (KHI) (Yoon & Drake 1996; Shinohara et al. 2001), which arises from the velocity shear between the fast-drifting plasmas in the current sheet and the background plasmas, is of importance because of its significant modulation, and it enhances the magnetic diffusion rate by the LHDI (Shinohara et al. 2001). Recently the drift kink instability (DKI) (Zhu & Winglee 1996; Pritchett et al. 1996) and its cousin mode of the drift sausage instability (DSI) (Büchner & Kuska 1999; Yoon & Lui 2001; Silin & Büchner 2003) have been introduced. The DKI is a long-wavelength electromagnetic mode, which is driven by the fast-drifting plasmas in a thin current sheet and it quickly grows when the mass ratio of the positively charged particles to the electrons is small (Daughton 1998, 1999). Therefore the DKI smears out in geophysical ion-electron situations but the nonlinear development of the LHDI may lead to the current sheet modulation by the DKI (Horiuchi & Sato 1999). On the contrary, the DKI quickly grows in relativistic pair plasmas in which the mass ratio is the unity, while the LHDI smears out. Zenitani & Hoshino (2003, 2005a) investigated the DKI in relativistic current sheets of pair plasmas, and they found a dc particle acceleration along the neutral sheet in the nonlinear stage of the relativistic drift kink instability (RDKI). Because of its fast growth rate, the RDKI is one of the most likely processes in relativistic current sheets.

The purpose of this paper is to investigate basic physical properties of reconnection or reconnection-related processes in relativistic pair plasmas. Two types of two-dimensional problems, relativistic magnetic reconnection and the RDKI, are demonstrated by using fully electromagnetic PIC simulations. In addition, based on the obtained theories we discuss possible application to the Crab pulsar wind problem.

This paper is organized as follows. In §2 we describe our simulation setup. In §3 a two-dimensional simulation study of relativistic magnetic reconnection is presented. In §4

another two-dimensional study of the RDKI is presented. In §5 we compare the two results and discuss the possible application to the pulsar winds.

2. Simulation

2.1. Simulation method

The simulation is carried out by a three-dimensional electromagnetic PIC code. In this code we solve the following basic equations: the relativistic equation of motion

$$\frac{d}{dt}(m_j\gamma_j\mathbf{v}_j) = q_j\left(\mathbf{E} + \frac{\mathbf{v}_j}{c} \times \mathbf{B}\right) \quad (1)$$

$$\frac{d}{dt}\mathbf{x}_j = \mathbf{v}_j \quad (2)$$

and the Maxwell equations

$$\nabla \times \mathbf{B} = \frac{4\pi}{c}\mathbf{j} + \frac{1}{c}\frac{\partial}{\partial t}\mathbf{E} \quad (3)$$

$$\nabla \times \mathbf{E} = -\frac{1}{c}\frac{\partial}{\partial t}\mathbf{B} \quad (4)$$

$$\nabla \cdot \mathbf{B} = 0 \quad (5)$$

$$\nabla \cdot \mathbf{E} = 4\pi\rho \quad (6)$$

where \mathbf{x}_j , \mathbf{v}_j , γ_j , m_j , and q_j are the position, the velocity, the Lorentz factor, the rest mass, and the charge for the j -th super-particle in the simulation system. The charge density ρ and the current density \mathbf{j} are obtained by

$$\rho = \sum_j q_j S(\mathbf{x}_j) \quad (7)$$

$$\mathbf{j} = \sum_j q_j \mathbf{v}_j S(\mathbf{x}_j) \quad (8)$$

where \sum denotes integration in the cell and $S(x)$ is the shape function of the super-particles. For simplicity, we do not consider any collisions, radiation, pair production, or pair annihilation of electron-positron plasmas.

2.2. Initial configuration

As an initial configuration, we use a relativistic Harris configuration (Kirk & Skjæraasen 2003; Harris 1962). In the Cartesian coordinate system, magnetic field and plasma distribu-

tion functions are

$$\mathbf{B} = B_0 \tanh(z/\lambda) \hat{\mathbf{x}}, \quad (9)$$

$$f_s = \frac{n_0 \cosh^{-2}(z/\lambda)}{4\pi m^2 c T K_2(mc^2/T)} \exp\left[\frac{-\gamma_s(\varepsilon - \beta_s m c u_y)}{T}\right] + \frac{n_{bg}}{4\pi m^2 c T_{bg} K_2(mc^2/T_{bg})} \exp\left[-\frac{\varepsilon}{T_{bg}}\right], \quad (10)$$

where λ is the thickness of the current sheet, the subscript s denotes the species (plus signs for positrons and minus signs for electrons), n_0 is the plasma number density of the current sheet in the proper frame, T is the plasma temperature including the Boltzmann constant, $K_2(x)$ is the modified Bessel function of the second kind, $c\beta_s$ is the drift speed of the species, and u is the four-velocity. Throughout this paper we set $\beta_+ = 0.3$ and $\beta_- = -0.3$ and therefore $\gamma_\beta = 1.048$. The n_{bg} is the number density of background plasmas, and T_{bg} is its temperature including the Boltzmann constant. The pressure balance condition and the current condition are satisfied in the equilibrium state;

$$B_0^2/8\pi = 2d_0 T/\gamma_\beta = 2n_0 T \quad (11)$$

$$cB_0/(4\pi\lambda) = \sum_s \gamma_s q_s n_s v_s = 2en_0 \gamma_\beta c\beta = 2ed_0 c\beta, \quad (12)$$

where $d_0 = \gamma_\beta n_0$ is the plasma density in the laboratory frame.

In the Harris system, we can take two free parameters. We employ the temperature T and the drift speed parameter β . The temperature T is a measure of the relativity in this study. In the nonrelativistic regime, one can obtain the typical Alfvén speed V_A in the system from equation (11).

$$V_A \sim \frac{B_0}{\sqrt{4\pi m(2n_0)}} = \sqrt{2} \left(\frac{T}{mc^2}\right)^{1/2} c \quad (13)$$

Therefore, the typical Alfvén speed becomes on the order of c and then several relativistic effects appear, when $T \gtrsim mc^2$. The drift speed parameter β also stands for the current sheet thickness. Combining equations (11) and (12), one can obtain the Debye length λ_D ,

$$\lambda_D = \sqrt{\frac{T}{4\pi d_0 e^2 \gamma_\beta}} = \beta \cdot \lambda. \quad (14)$$

The typical gyroradius r_L in the $T \gg mc^2$ limit can be approximated as

$$r_L \sim \left(\frac{eB_0}{\gamma mc}\right)^{-1} c = \frac{(T/\gamma_\beta) mc^2}{mc^2 eB_0} = (\beta/2\gamma_\beta) \cdot \lambda. \quad (15)$$

In the nonrelativistic limit of $T \ll mc^2$,

$$r_L = \left(\frac{eB_0}{mc}\right)^{-1} v_{th} = \frac{mc}{eB_0} \sqrt{\frac{2T}{m\gamma_\beta}} = \frac{\beta}{\sqrt{2\gamma_\beta}} \left(\frac{T}{mc^2}\right)^{-1/2} \cdot \lambda, \quad (16)$$

where v_{th} is the thermal velocity of plasmas.

We use the three-dimensional PIC code. The system size is set to $1024 (x) \times 1 (y) \times 512 (z)$ in reconnection studies and $1 (x) \times 256 (y) \times 512 (z)$ in drift kink studies. We consider periodic boundaries in the x -, y - and z -directions. Since the magnetic field lines change their directions in a current sheet, we set two simulation domains in the z direction: one domain for the first Harris sheet and the other for the second Harris sheet, which has the same physical properties in the opposite directions. Usually, physical processes are investigated in the first half (bottom half) of the whole simulation box, and so the effective size in z is 256 grids. The typical scale of the current sheet λ is set to 10 grids. Therefore, the boundaries are located at $x = \pm 51.2\lambda$ (reconnection) or at $y = \pm 12.8\lambda$ (drift kink). The z -boundaries of the main simulation domain are located at $z = \pm 12.8\lambda$. Simulation time is normalized by the light transit time $\tau_c = \lambda/c$.

A list of simulation runs is presented in Table 3. Note that $\omega_c = eB_0/mc$ means “unit gyroradius”. In the relativistic limit, the typical gyroradius becomes larger by a factor of T (eq. [15]).

3. Relativistic magnetic reconnection

3.1. Simulation result

First, we present our simulation study of relativistic magnetic reconnection. The system size is $1024 (x) \times 1 (y) \times 512 (z)$, and the physical size of the main simulation box is $-51.2 < x/\lambda < 51.2$, $-12.8 < z/\lambda < 12.8$. The plasma temperature is set to $T/mc^2 = 1.0$, so that the system’s typical Alfvén speed is $V_A \sim 0.53c$. The background plasma temperature T_{bg} is set to $0.1mc^2$. We call this run run R3 in Table 3. In order to trigger an X -type neutral line around the center of the simulation box, we add artificial electric fields in the very early stage of the simulation. We assume the triggering electric field E_{trig} and its maximum amplitude, typical location, and duration time are $0.3B_0(V_A/c)$, $(x \pm \Delta x, z \pm \Delta z) = (0 \pm 2, 3 \pm 1)$, and $10\lambda/V_A$, respectively. During $0 < t < \tau_{trig}$, we force $E_y \geq E_{trig}$ so that plasmas enter the X point. Its duration $10\lambda/V_A \sim 10 - 15\tau_c$ is short enough, compared with the total timescale of the simulation. Because of this modification the system slightly gains energy by 0.2% in the very early stage, and the total energy is conserved within 0.4% error until the end of the

simulation at $t/\tau_c = 300.0$.

The three panels in Figure 1 present the snapshots at $t/\tau_c = 60.0, 80.0$, and 100.0 . The color contour shows the density of plasmas, which is normalized by the original plasma sheet density $\rho_0 = 2\gamma_\beta n_0$. The solid lines represent magnetic field lines. The field lines are originally in the $+x$ direction on the upside of the current sheet and the $-x$ direction on the downside of the current sheet. Because of the triggering field, the field lines start to reconnect near the center of the simulation box. Along with the magnetic field lines, plasmas from the background region come into the X -type region and then they stream out as reconnection jets toward the $\pm x$ directions. The evolution looks like Sweet-Parker type reconnection with a flat current sheet structure. The average velocity of plasmas $\langle \mathbf{v} \rangle = \int f \mathbf{v} d\mathbf{u} / \int f d\mathbf{u}$ is up to $(0.8-0.9)c$ in the outflow regions and $(0.3-0.4)c$ in the inflow regions. The outflow speed exceeds the typical Alfvén speed in the system. At $t/\tau_c = 80.0$ and 100.0 , reconnected magnetic field lines (B_z) are swept away from the X -type region. As a result, the field lines are piled up around $x/\lambda = \pm 20$ or ± 30 in front of the dense plasma regions. After $t/\tau_c = 100.0$, the system is influenced by the periodic boundary conditions. Reconnection outflow jets come closer to the x -periodic boundaries at $x/\lambda = \pm 51.2$, where the plasma density starts to increase. In addition, the X -point starts to sweep magnetic flux from the other simulation box. At $t/\tau_c = 100.0$, the magnetic field lines at the X -point come from $z/\lambda \sim \pm 12-13$ around $x/\lambda = \pm 51.2$. Note that the z -boundaries are located at $z/\lambda = \pm 12.8$. Dense plasma regions are blown away from the center, they meet each other near the x -periodic boundaries. Then they merge into a single O -point, and the O -point starts to evolve in the vertical (z) direction. After that, the system evolves gradually to another relaxed state: vertical current sheets. Figure 2 is a snapshot in the late-time stage at $t/\tau_c = 300.0$. Both main ($-12.8 < z/\lambda < 12.8$) and sub ($12.8 < z/\lambda < 38.4$) simulation boxes are presented. The white rectangle indicates the region in the snapshots from Figure 1. The magnetic fields are antiparallel; $B_z < 0$ in the left half ($z/\lambda < 0$) and $B_z > 0$ in the right half ($0 < z/\lambda$), but at present we do not observe the secondary magnetic reconnection in these vertical current sheets.

The panels in Figure 3 are energy spectra in the main simulation box. The vertical axis shows the count number of super particles on a log scale, and the horizontal axis shows particle's energy which is normalized by the rest-mass energy mc^2 . The bottom panel of Figure 3 presents the energy spectra in double-log format. The spectrum labeled by $t/\tau_c = 100.0'$ is the partial energy spectrum at $t/\tau_c = 100.0$, which is integrated near the central region of $-12.8 < x/\lambda < 12.8$. After the reconnection breaks up, the high-energy tail rapidly grows in time. This is due to the dc particle acceleration around the X -point (Zenitani & Hoshino 2001) and we discuss the acceleration mechanism in more detail in §3.2. The slope of the spectrum at $t/\tau_c = 80.0$ is well approximated by the power-law distribution with an

index of -3.1 to -3.2 in the range of $10 < \varepsilon/mc^2 < 50$. This is consistent with the other study; Jaroschek et al. (2004) obtained a spectral index of -3 in their PIC simulations with lower temperature $T/mc^2 = 0.2$. At $t/\tau_c = 100.0$, the spectrum seems to have a double power-law shape, whose hardest slope is roughly approximated by the index of -2.4 . The partial energy spectrum at $t/\tau_c = 100.0$ looks harder. Finally, the maximum energy is up to $150mc^2$. The late-time state at $t/\tau_c = 300.0$ also has its spectral index of -2.4 .

The panels in Figure 4 show the electric field structure at $t/\tau_c = 80.0$ and 100.0 . Because of the symmetry, we present two properties, $(E^2 - B^2)$ in the left halves ($x/\lambda < 0$) and the reconnection electric field E_y in the right halves ($0 < x/\lambda$). The white contour lines are drawn by 0.25. Since the reconnection magnetic fields (B_x or B_z) are small near the X -type region and since the reconnection electric field E_y is finite, $(E^2 - B^2)$ becomes positive inside the narrow sheet region around the X -type region; $-10 < x/\lambda < 10$ at $t/\tau_c = 80.0$ and $-15 < x/\lambda < 15$ at $t/\tau_c = 100.0$. The reconnection electric field E_y is almost constant around the X -type region: $E_y/B_0 \sim 0.2$ at $t/\tau_c = 80.0$ and $E_y/B_0 \sim 0.15$ at $t/\tau_c = 100.0$. There are strong peaks around $x/\lambda = \pm 20$ at $t/\tau_c = 80.0$, $x/\lambda = \pm 30$ at $t/\tau_c = 100.0$. These regions are identical to the magnetic pile-up regions, where the reconnected magnetic field lines are compressed in front of the dense current sheet regions. The electric fields E_y are enhanced due to the motional electric field of the magnetic piled-up flux. The other two components (E_x and E_z) are negligible.

3.2. Particle acceleration

Next, we look at the particle acceleration in relativistic reconnection. In order to analyze how and where the nonthermal particles are accelerated, we pick up high-energy particles whose energy exceeds $50mc^2$ at $t/\tau_c = 100.0$. The panels in Figure 5 show their spatial distribution at three different stages. At $t/\tau_c = 40.0$, some particles are near the X -type region and other particles are widely scattered in the background region. Importantly, they stay around or move into the X -type region at $t/\tau_c = 60.0$, when the reconnection breaks up. The nonthermal tail in the energy spectra starts to grow in this stage. As the reconnection evolves, they are spread over the thin current sheet, and then some of them are ejected from the reconnection region. The acceleration site is obviously the central region in and around the X -type region. Looking at the electromagnetic fields near the acceleration site in panels in Figure 4, we note that the electric fields are relatively stronger than the magnetic fields.

We call the central region that satisfies $(E^2 - B^2) > 0$ the “acceleration region” (AR), where the electric field is dominant. In two-dimensional reconnection, $(E^2 - B^2) > 0$ is equivalent to our old definition of the AR: $|E_y| > |B_x^2 + B_z^2|$ in Zenitani & Hoshino (2001)

(hereafter ZH01). Such an AR does not have a de Hoffman-Teller frame. For example, let us consider an electromagnetic field $\mathbf{B}(0, 0, B_z), \mathbf{E}(0, E_y, 0)$ near the X -points along the neutral sheet ($z = 0$). The fields can be transformed into

$$\mathbf{B}(0, 0, B_z), \mathbf{E}(0, E_y, 0) \rightarrow \begin{cases} \mathbf{B}'(0, 0, B_z/\gamma_{v_1}), \mathbf{E}'(0, 0, 0) & (|E_y| < |B_z|) \\ \mathbf{B}'(0, 0, 0), \mathbf{E}'(0, E_y/\gamma_{v_2}, 0) & (|E_y| > |B_z|) \end{cases} \quad (17)$$

where the prime is for the transformed properties, $v_1/c = E_y/B_z$ and $v_2/c = B_z/E_y$ are the transformation speeds, and γ_{v_1} and γ_{v_2} are the relevant Lorentz factors. Generally, when the Lorentz invariant ($E^2 - B^2$) is positive, the electric field cannot be removed and the particle motion in the AR is controlled by the electric field in the transformed frame. In the observer's frame, particles are driven into some y -aligned direction, gaining their energy through the reconnection electric field E_y . So, once particles enter the acceleration site, they are driven by the electric field E'_y inside the AR and they travel through (relativistic) Speiser orbits (Speiser 1965) outside the AR. The AR looks thinner in z compared with ZH01, but the thickness of the AR does not provide significant change because the magnetic field B_x confines particles near the neutral sheet in a reconnection configuration. In ZH01, we estimate that the energy distribution in the AR can be approximated by the power law distribution, whose index is on the order of -1 . Although it is difficult to evaluate the partial energy spectra in the AR by power law, the index is between -2 and -1 in Figure 3.

In the bottom panel of Figure 5, the red spots present 33 particles, whose energy exceeds $90mc^2$ at $t/\tau_c = 100.0$. They are found only near the magnetic pileup regions along the flat current sheet layer. According to the partial and the main energy spectra at $t/\tau_c = 100.0$ in Figure 3, the intermediate-energy particles ($40mc^2 < \varepsilon < 70mc^2$) are found both inside and outside the selected region and their spectral slopes look similar. The selected region has fewer intermediate-energy particles by a factor of 3, because the region is narrower than the typical current sheet length. On the contrary, high-energy particles whose energy exceeds $\varepsilon > 80mc^2$ are only found outside the selected region. Therefore, these highest energy particles are accelerated outside the selected region of $-12.8 < x/\lambda < 12.8$. In fact, during $t/\tau_c = 60.0$ and 80.0 , the highest-energy shoulder increases by $\Delta\varepsilon \sim (25 - 30)mc^2$, and some particles apparently gain more energy than the maximum energy gain inside the AR, $\Delta\varepsilon \sim (eE_y c \cdot 20\tau_c) \sim 25mc^2$, where we use $E_y \leq 0.2B_0$ as the typical value. Then, we traced the most energetic positron, whose energy is $97mc^2$ at $t/\tau_c = 100.0$ and who is found at $(x/\lambda, z/\lambda) = (31.0, -0.64)$. Its trajectory and xz -/ xy - projections are presented in Figure 6. Labels in the xy plane indicate the relevant times. Time histories of the relevant properties are presented in Figure 7, too. Originally, the positron's motion is well explained by the meandering motion; it bounces around the neutral sheet in the $\pm z$ direction. Around $t/\tau_c = (40 \sim 50)$, the reconnection breaks up and the positron enters the X -type region ($x/\lambda \sim 0$). Then, it is driven by the reconnection electric field E_y and its energy starts

to increase. In the gray background regions, the field satisfies the condition of the AR, $(E^2 - B^2) > 0$. This particle does not always stay in the AR, because it travels near the edge of the AR. After $t/\tau_c = 65$, the positron departs from the central AR and then it starts to travel through the (relativistic) Speiser orbit. The energy already reaches up to $\varepsilon = 50mc^2$ through particle acceleration in/near the central AR. At this stage, the positron's Larmor radius is $(\gamma mc^2/eB_0) \sim 8\lambda$. Because of a relativistic inertia effect, it can travel a longer distance into the y -direction through Speiser orbit. If we observe this particle in the moving frame of the plasma outflow, its energy stays nearly constant after $t/\tau_c \gtrsim 65$. In the simulation frame, the particle gains further energy from E_y until it is ejected into the x -direction.

Interestingly, in this case the particle gains more energy than the standard Speiser orbit case, because the electric field E_y increases in time at the particle's position. Figure 8 is an x - t diagram of the positron's position and the E_y -profile. The dashed line presents the positron trajectory, and the stack plots show the time development of the reconnection electric field E_y along the neutral sheet ($z = 0$). Surprisingly, the positron always stays around the peak of the electric field E_y , which is related to the magnetic pile-up region. Since magnetic field lines are continuously transported from the X -type region, the piled-up peak increases in its height, and then E_y is further enhanced by the relevant motional electric field. In other words, the particle speed resonates with the propagating speed of the reconnection pileup front $\sim 0.6 - 0.7c$, which is slightly slower than the reconnection outflow speed. In the geophysical ion-electron contexts, Birn et al. (1997) studied ion acceleration and Hoshino et al. (2001) studied electron acceleration in the magnetic dipole/pileup regions. In both cases, particles gain their energy from E_y , through $\nabla \mathbf{B}$ drift motion in the y -direction. In our case, the particle directly resonates with the fields. In order to stay for a long time in the piled-up front, the particle has to be heavy enough or the particle's Larmor radius has to be large enough. Therefore, only high-energy particles can be continuously accelerated to the highest energy; most of them are preaccelerated around the AR when they enter the piled-up regions. Low-energy particles are quickly ejected into the outflow directions. When these pileup regions hit the downstream dense regions, it releases a lot of energy into the downstream plasma energy. The downstream plasmas increase their energy on the order of $\Delta\varepsilon \sim 2r'_L eE'_y \sim 3(\gamma mc^2/eB_0)eB_0 \sim 3\gamma mc^2$, where the prime denotes the physical properties in the piled-up front frame, and this mirror effect explains the mild enhancement of the global energy spectra around $\varepsilon \sim (20 - 30)mc^2$. If we compare the piled-up region with the AR, the piled-up region mainly contributes to the plasma heating, but it also enhances the maximum energy of a small number of highly accelerated particles. A similar mechanism is reported in Jaroschek et al. (2004), although their difference between the dc acceleration in the central AR and this piled-up acceleration was not clear. Their system becomes highly

turbulent, because the main reconnection is suppressed by the conductive wall boundary effect in the inflow region. On the contrary, in our case, the main reconnection is so powerful that it sweeps out everything into the $\pm x$ direction, including small tearing islands in its early stage. Therefore, the acceleration continues for a longer time, until outflow jets reach the periodic boundaries. We do not know how long the single reconnection region can dominate, but we remark that the higher maximum energy will be obtained when a single reconnection dominates.

Figure 9 summarizes the acceleration mechanism, presenting the electromagnetic field properties at $t/\tau_c = 100.0$ along the neutral plane $z = 0$. As stated, the electric field is larger than the magnetic field B_z near the X -type region $x/\lambda < 14$, while B_z exceeds E_y in $x/\lambda > 14$. The dashed line presents the ratio of E_y to B_z , which agrees with the plasma outflow speed around the outflow the region. In this figure, we can classify the acceleration site into the following three types:

Central acceleration region —Where $(E^2 - B^2) > 0$ and dc direct acceleration takes place.

Outside region —Where $(E^2 - B^2) < 0$ and particles are accelerated through the (relativistic) Speiser orbit.

Magnetic pileup region —Where some high-energy particles resonate with the enhanced electric field.

Regarding the boundary effects on the late-time development, the plasma collision across the x -boundaries enhances the magnetic pileup flux and the relevant acceleration. However, such a collision is quite likely to occur in realistic situations. For example, the coalescence of multiple reconnection islands have recently attracted our attention because it generates energetic particles (Saito & Sakai 2006). Since our system width ($L_x = 102.4\lambda$) is rather larger than the typical scale of the tearing mode ($\sim 20\lambda$, assuming that the fastest mode is $k_x\lambda \sim 0.3$), we believe that the x -boundary effect is plausible. The z -boundary effect may be rather artificial; however, it is unlikely that the z -boundary effect accelerates the reconnection process in the early stage of $t/\tau_c \lesssim 100$. The inflow magnetic flux continually decreases in time (approximately half of the original flux $\sim 0.5B_0$ at $t/\tau_c = 100.0$) and then it starts to increase in the later stages at $t/\tau_c \gtrsim 170$, due to the O -point expansion in the sub simulation domain. In the striped pulsar wind condition, it is possible that double/multiple current sheets are close to each other. Since we note that the late-time energy spectra become even harder (with an index of ~ -2.4), these results imply that harder energy spectra may be generated when the pulsar wind is crowded by the multiple current sheets. Of course, it is very difficult to discuss the spectral index from the simulation results, because it shows the

very early development in a small region compared with actual astrophysical phenomena. It just gives us a hint to discuss an astronomical long-time/large-scale evolution and the resulting energy spectra.

3.3. Case studies

We have further carried out five simulation runs with different temperature parameters; $T/mc^2 = 16, 4, 1, 1/4$ and $1/16$. We call them runs R1-R5 and their parameters are presented in Table 3. The background plasma temperature T_{bg} is always set to $0.1T$ and $n_{bg}/(\gamma_\beta n_0)$, the ratio of the number density in the simulation frame, is fixed to 0.05. The amplitude and duration of triggering fields are selected case by case, but we usually use smaller values than run R3. For comparison, our previous work (ZH01) is presented as run R0, whose parameters are equivalent to $T/mc^2 \sim 1/4$ and $\beta \sim 0.27$.

The results of the parameter studies are presented in Figures 10, 11, and 12 and Table 1. Figure 10 shows typical snapshots in runs R1 and R5 ($T/mc^2 = 16$ and $1/16$). The energy spectra in run R1 are also presented in Figure 11. The enhancements of plasma kinetic energies in runs R1-R5 are presented in Figure 12a. Their energies are normalized by the plasma pressure energy in the original current sheet, which is roughly proportional to the temperature T . The time axis is re-arranged so that reconnection breaks up nearly at the same time. In addition, in order to evaluate the acceleration amplitude, we calculate the “nonthermal ratio” index of K_{nth}/K in Figure 12b, where K is the total kinetic energy in the main simulation box and K_{nth} is its nonthermal part. We estimate K_{nth} by comparing the energy spectra and its equivalent “thermal” distribution. Its derivation is described in Appendix A. Figure 12c presents the size of the acceleration region in the main simulation box, which satisfies the condition of $(E^2 - B^2) > 0$. Table 1 shows characteristic speeds in the system. We pick up the maximum plasma speed along outflow/inflow regions, as long as it does not violate the MHD frozen-in condition so much. The typical Alfvén velocity is calculated from the background magnetic field B_0 and plasma parameters in the current sheet (n_0, T). The inflow Alfvén velocity is the local Alfvén speed in the background region.

System evolutions are quite similar in relativistic cases of $T/mc^2 \gtrsim 1$. In run R1, the spatial structure (Fig. 10a) and the power-law index of -3.2 (Fig. 11) in the reconnection phase are in good agreement with those of run R3. In the very late time stage (at $t/\tau_c = 314.0$), the power-law index is approximately -2.4 . The evolution timescale of $(30-50)\tau_c$ and the saturation level (Fig. 12a) and a portion of the nonthermal energy (Fig. 12b) are almost the same, too. The ratio of the inflow speed and the outflow speed usually stay around 0.3-0.4, except for run R1 (Table 1). In run R1, the rate becomes slightly higher due to the faster

inflow speed. However, it still stays nonrelativistic; the relevant Lorentz factor is only ~ 1.25 , and the typical inflow speed is slower because we picked up the highest inflow speed along the y axis. Considering that the system is magnetically dominated $[(B_0^2/8\pi)/(\sum \varepsilon) \sim 60]$ in the inflow region and that the reconnection layer’s aspect ratio is $L/\delta \sim 10$, where L and δ are the typical width and height of Sweet-Parker reconnection layer, our results do not agree with Lyutikov & Uzdensky (2003); they predicted that the inflow velocity becomes relativistic and that the outflow velocity is faster than the inflow Alfvén speed when the inflow region is magnetically dominated.

In less relativistic cases, the current sheet structure is ambiguous or diffusive (Fig. 10*b*). This is due to relatively large Larmor radius (eq. [16]; $r_L \sim 0.8\lambda$ in run R5) in the non-relativistic limit. In addition, the system evolves slowly because of the slower characteristic speed: the nonrelativistic Alfvén speed. Contrary to relativistic MHD simulations (Watanabe & Yokoyama 2006), in which the outflow speed is well-approximated by the inflow Alfvén speed, the maximum outflow speed stays between the two Alfvén speeds. The size of the AR decreases and then fewer nonthermal particles are observed. Strictly speaking, this may contain ARs in several X -points or magnetic nulls inside the O -points. However, in the breakup stage of reconnection ($50 < t/\tau_c < 100$), they represent the size of the AR in the single reconnection region very well. We believe that the size of the AR is controlled by the reconnection outflow speed. The magnetic topology of reconnection is rather insensitive to parameters and so the relative size of the AR depends on the amplitude of the reconnection electric field E_y . Then, E_y is controlled by the typical outflow speed through the frozen-in condition at the outflow region, $|v_{out}| = c|E_y|/|B_{z0}|$, where B_{z0} is the typical reconnected magnetic field. In summary, in the relativistic regime, the AR (Fig. 12*c*) becomes larger due to its relativistic outflow speed v_{out}/c , and then reconnection generates more nonthermal particles (Fig. 12*b*).

The direct acceleration around the AR is not likely to occur in the solar flare regions or the Earth’s magnetotail, where the reconnection outflow is on the order of the Alfvén speed of 10^6 (m/s) $\ll c \sim 3 \times 10^8$ (m/s) and the AR is restricted within the electron inertial length.

4. Relativistic drift kink instability

4.1. Simulation result

Next, we introduce the other two-dimensional simulations in the y - z plane. The system size is now set to 1 (x) \times 256 (y) \times 512 (z). We set no artificial electric fields to excite instabilities, since instabilities spontaneously arise from thermal noise. We set no background

plasmas. In the first simulation, we set $T = mc^2$. This run is run D3 in Table 3.

Characteristic snapshots of the simulation are presented in Figure 13. The color contours shows the plasma density, which is normalized by the peak density of the Harris current sheet $\rho_0 = 2\gamma_\beta n_0$. Figure 14 presents the energy spectra at the corresponding times. Figure 15 presents the electric structures of selected stages. The left three panels of Figure 15 are color contours of the electric field E_y . The sign of E_y is positive in light gray (yellow) regions, while it is negative in dark gray (blue) regions. The right panels of Figure 15 show the electric field E_z at the corresponding time. White lines are contours of B_x , whose structure is similar to the density profile.

After tens of the light transit time, we observe a linear growth of a kink-type structure around $t/\tau_c = 46.0$. This is due to the relativistic drift kink instability (RDKI) (Zenitani & Hoshino 2005a), a relativistic extension of the drift kink instability (DKI), which is a long-wavelength, current-driven instability in a thin current sheet. In the top panels in Figure 15, one can see a typical structure of the polarization electric fields of E_y and E_z at this stage. The E_y plot in the top left panel shows two types of color regions along the current sheet: yellow means $E_y > 0$ or in the right direction and blue means $E_y < 0$ or in the left direction. They are anti-symmetric with the neutral plane ($z = 0$). Since B_x is positive on the upside of the current sheet and negative on the downside of the current sheet, the observed sign of $\mathbf{E} \times \mathbf{B}$ is consistent with the z -displacement of the plasma bulk motion. The other components of electromagnetic fields, E_x , B_y , and B_z , are negligible. After $t/\tau_c \sim 50$, the system turns into its nonlinear stage. The typical signature is presented at $t/\tau_c = 64.0$ in Figures 13, 14, and 15. In this stage, the current sheet is strongly modulated by the RDKI around $-4 < z/\lambda < 4$. Because of the z -displacement by the RDKI, we see the characteristic regions in a row along neutral plane ($z = 0$) in the middle left panel of Figure 15. Originally, these regions were alternately arranged on the upper side and on the lower side of the neutral plane in the top left panel of Figure 15. Importantly, we observe a clear sign of the particle acceleration in high-energy tails in the energy spectra in Figure 14. We discuss the acceleration process later.

After the nonlinear development, the folded current sheets start to collapse each other, and then the system turns into the “mixed” stage. Typical signatures are presented in snapshots at $t/\tau_c = 82.0$ in Figures 13, 14 and 15. Particle acceleration seems to stop because the acceleration channel structure disappears. Because of the collisions of sheet fragments, magnetic energy is diffused into plasma heat, and then the total kinetic energy has increased by 170% at this time. Finally, the mixed current sheet slowly evolves into the broadened current sheet, which is 3 or 4 times thicker than the initial sheet width. The signature of this stage is presented in the snapshots at $t/\tau_c = 200.0$ in Figures 13 and

14. The spectrum looks unchanged from the mixed stage; one can still see the remnant of the nonthermal tail. We still recognize both a remnant of the nonthermal tail and heated plasma component in the spectrum at $t/\tau = 200.0$ in Figure 14. Throughout Run D3, the total energy is conserved within an error of 0.3%.

4.2. Linear analysis

Throughout the simulation run, we have observed the perturbed magnetic field δB_x in the neutral plane ($z = 0$). We have examined the periodic perturbation modes and their time histories are presented in Figure 16. Each mode (2-5) corresponds to $k_y\lambda = 0.49, 0.74, 0.98$, and 1.22, respectively. The most dominant mode is mode 4 with $k_y\lambda = 0.98$. Its linear growth rate is $\omega_i \sim 0.11\tau_c^{-1}$ or $\omega_i \sim 0.035\Omega_c$, where $\Omega_c = \omega_c/\gamma = (eB)/(\gamma mc^2)$ is the typical gyro frequency.

Pritchett et al. (1996) (hereafter P96) analyzed the linear stability of the DKI with fluid equations and Maxwell equations. We employed a similar method to our case with the relativistic fluid equation

$$\frac{\gamma_s^2}{c^2}(p_s + \varepsilon_s)\left(\frac{\partial}{\partial t} + \mathbf{v}_s \cdot \nabla\right)\mathbf{v}_s = -\nabla p_s + \gamma_s q_s n_s \left(\mathbf{E} + \frac{\mathbf{v}_s}{c} \times \mathbf{B}\right) - \frac{\mathbf{v}_s}{c^2}(\gamma_s q_s n_s \mathbf{E} \cdot \mathbf{v}_s + \frac{\partial p_s}{\partial t}), \quad (18)$$

the particle conservation law

$$\frac{\partial}{\partial t}(\gamma_s n_s) + \nabla \cdot (\gamma_s n_s \mathbf{v}_s) = 0, \quad (19)$$

and adiabatic gas condition with polytropic index $\Gamma = 4/3$

$$p_s \propto n_s^\Gamma. \quad (20)$$

The polytropic index Γ should go down to 5/3 in the nonrelativistic limit; however, setting $\Gamma = 5/3$ provides no significant change in our calculation. The detailed formulation is presented in Appendix B. We have to be careful because the typical scale of particle motions are comparable to the plasma sheet thickness: the gyroradius $c/(eB/\gamma mc) \sim 0.3\lambda$ or the meandering width $[(c/\Omega_c)\lambda]^{-1/2} \sim 0.6\lambda$. Therefore, fluid theory and the adiabatic gas condition are no longer valid in small scale structures. In addition, the theory is less trustable when we choose a larger β parameter, because the typical gyro scale becomes larger (eq. [15]). The eigenprofiles for $k_y\lambda = 1.0$, which is close to the most dominant mode (mode 4; $k_y\lambda = 0.98$) in run D3, are presented in Figure 17. In the top panel in Figure 17, perturbations of the magnetic field (δB_x) and the electric fields (δE_y and δE_z) are shown as functions of z . They are normalized by the maximum amplitude of δB_x . The anti-symmetric

structure of δE_y corresponds to the positive and negative E_y regions along the neutral plane ($z = 0$). The other three components ($\delta B_y, \delta B_z, \delta E_x$) are zero in this case. The z -profiles of velocity perturbations are presented in the middle panel in Figure 17. The parameters $\delta V_{y\pm} = \delta v_{yp} \pm \delta v_{ye}$ and $\delta V_{z\pm} = \delta v_{zp} \pm \delta v_{ze}$ show the bulk or relative motion of the two species. The x components of the velocity perturbations ($\delta v_{x\{p,e\}}$) are zero. The plasma bulk motion in the z -direction, $\delta V_{z+} = \delta v_{zp} + \delta v_{ze}$, is dominant around the neutral plane. The relative z -motion $V_{z-} = \delta v_{zp} - \delta v_{ze}$ is also dominant around the neutral plane. It is mainly due to z -projection of the original counter-streaming current. A small-scale structure around $|z/\lambda| \sim 2 - 3$ may be numerical noise, which we could not completely clear out. The bottom panel in Figure 17 shows the density perturbation of $\delta D_{\pm} = \delta d_p \pm \delta d_e$, where $d = \gamma n$ is the plasma density in the observation frame. The anti-symmetric structure of δD_+ is consistent with the z -displacement of the central current sheet. Generally, their structures are in good agreement with the obtained simulation data, except for unphysical small structures (i.e. small waves in $i\delta V_{y+}$ around $z/\lambda = \pm 2.5$). The perturbation profiles in the simulation at $t/\tau_c = 40.0$ and the eigen functions are presented in Figure 18. The left panel compares mode 2 ($k\lambda = 0.49$) in simulation and eigen mode for $k\lambda = 0.50$. Both are in excellent agreement, although δE_y in simulation looks slightly noisy because of its weak amplitude. The right panel of Figure 18 compares mode 4 ($k\lambda = 0.98$) and eigen mode for $k\lambda = 1.00$. They are in good agreement in δB_x , while δE_y in simulation is approximately half of the eigen profile. The difference is also found in their the growth rates; the eigen growth rate at $k\lambda \sim 1.0$ is $\omega_i = 0.19\tau_c^{-1}$. We believe the fluid instability is dumped by the kinetic effect, or, in other words, fluid theory is losing its validity around the short wavelength of $k\lambda \gtrsim 1$. We discuss the validity of our theory later again. The charge separation (D_-) is schematically described in Figure 19. Once the current sheet is modulated, the streaming e^+ fluid and the counter-streaming e^- fluid are slightly separated in $\pm x$ direction, due to the particle inertia or the drift motion between the centrifugal force and magnetic fields. Then the separated charges produce the electrostatic fields E_y and E_z . Since the $E_y \times B_x$ motion enhances the current sheet modulation in the z direction, the instability continues to grow. There is no influence of the Kelvin-Helmholtz instability in the system. Since we set empty background plasmas, there is no velocity shear between the current sheet and the background region. We also compare run D3 and the other run with 5% of background plasmas (run D3a in Table 3), and we confirm that their growth rates are the same.

4.3. Analytical theory

Following P96, we construct a simple analytic solution of the instability in a long-wavelength limit and with $\beta \ll 1$. We drop the third term from the right-hand side of

equation (18), because they are smaller than other terms when linearized in a limit of $\beta \ll 1$. We get

$$\frac{(\mathbf{v}_s/c^2)(\gamma_s q_s n_s \delta \mathbf{E} \cdot \mathbf{v}_s)}{\gamma_s q_s n_s \delta \mathbf{E}} \sim O(\beta^2), \frac{(\mathbf{v}_s/c^2) \partial \delta p_s / \partial t}{\nabla \delta p_s} \sim O(\beta \frac{c_s}{c}) \lesssim O(\frac{\beta}{\sqrt{3}}), \quad (21)$$

where c_s is the sound speed. In addition, using the density ($n_s \gamma_s = d_s$) in the observer's frame and rewriting the enthalpy term $M = m \gamma_s (1 + [\Gamma/(\Gamma - 1)][T/(mc^2)])$, we obtain

$$M d_s \left(\frac{\partial}{\partial t} + \mathbf{v}_s \cdot \nabla \right) \mathbf{v}_s = -\nabla p_s + d_s q_s \left(\mathbf{E} + \frac{\mathbf{v}_s}{c} \times \mathbf{B} \right) \quad (22)$$

and the equation of continuity

$$\frac{\partial d_s}{\partial t} + \nabla \cdot (d_s \mathbf{v}) = 0. \quad (23)$$

Using P96's method (described in the Appendix in P96) in equations (22) and (23) and the Maxwell equations, one can obtain the modified growth rate of the DKI,

$$\gamma_{RDKI}/(k_y c \beta) \approx 1 - 2 \left(\frac{c \beta}{(e B_0 / M c) \lambda} \right) k_y \lambda = 1 - 2 \gamma_\beta \left(1 + \frac{\Gamma}{\Gamma - 1} \frac{T}{m c^2} \right) \left(\frac{c \beta}{(e B_0 / m c) \lambda} \right) k_y \lambda, \quad (24)$$

where γ_{RDKI} is the growth rate of the RDKI. Since equation (24) gives larger results than the actual growth rates in nonrelativistic studies (Pritchett et al. 1996; Daughton 1999), we assume that its right-hand side of the equation gives an upper limit of the growth rate. Using equations (11) and (12), we obtain γ_{RDKI} as a function of $k_y \lambda$,

$$\tau_c \gamma_{RDKI} \approx [1 - \gamma_\beta \left(\frac{m c^2}{T} + \frac{\Gamma}{\Gamma - 1} \right) \beta^2 (k_y \lambda)] \cdot \beta (k_y \lambda). \quad (25)$$

This equation has a maximum value

$$\tau_c \gamma_{RDKI} = \frac{1}{4 \gamma_\beta \beta} \left(\frac{m c^2}{T} + \frac{\Gamma}{\Gamma - 1} \right)^{-1} = \begin{cases} (4 \gamma_\beta \beta)^{-1} (T / m c^2) & (T \ll m c^2) \\ (16 \gamma_\beta \beta)^{-1} & (T \gg m c^2) \end{cases} \quad (26)$$

at

$$k_y \lambda = \frac{1}{2 \gamma_\beta \beta^2} \left(\frac{m c^2}{T} + \frac{\Gamma}{\Gamma - 1} \right)^{-1} = \begin{cases} (2 \gamma_\beta \beta^2)^{-1} (T / m c^2) & (T \ll m c^2) \\ (8 \gamma_\beta \beta^2)^{-1} & (T \gg m c^2) \end{cases}. \quad (27)$$

Thus, as long as $k_y \lambda < 1$ is satisfied in equation (27), equation (26) gives a plausible upper limit of γ_{RDKI} . In addition, equations (26) and (27) can be rewritten as

$$\tau_c \gamma_{RDKI} < (k \lambda_y / 2) \beta < \beta. \quad (28)$$

When $k_y\lambda \gtrsim 1$ in equation (27), we use $k_y\lambda = 1$ in equation (25) to obtain a plausible extension of the upper limit, considering that the original equation (24) is no longer valid in $k_y\lambda \gtrsim 1$. We have

$$\tau_c\gamma_{RDKI} = [1 - \gamma_\beta \left(\frac{mc^2}{T} + \frac{\Gamma}{\Gamma - 1} \right) \beta^2] \cdot \beta = \begin{cases} [1 - \gamma_\beta \beta^2 (mc^2/T)]\beta & (T \ll mc^2) \\ (1 - 4\gamma_\beta \beta^2)\beta & (T \gg mc^2) \end{cases} \quad (29)$$

Note that both equations (28) and (29) satisfy the simple condition

$$\tau_c\gamma_{RDKI} < \beta. \quad (30)$$

Figure 20 compares the linear growth rate of the instability in units of the light transit time of $\tau_c = \lambda/c$ (*left axis*) or the typical gyro frequency Ω_c (*right axis*), as a function of the normalized wavenumber ($k_y\lambda$). The calculated eigen growth rates, the analytical estimate (eq. [25]) and the observed growth rates in the simulations are presented. The observed growth rates correspond to modes 2-5 in Figure 16. We discuss the RDSI line in §4.4. The three values are in good agreement when $k_y\lambda \lesssim 0.7$. In shorter wavelengths of $k_y\lambda \gtrsim 1$, the simulation results do not agree with the theories because the instability is suppressed by kinetic effects. Daughton (1999) investigated the nonrelativistic DKI using Vlasov code, and his result also agreed with the fluid theory, when $k_y\lambda \lesssim 0.7$.

4.4. Relativistic drift sausage instability

The RDSI line in Figure 20 stands for the relativistic extension of the drift sausage instability, a cousin mode of the drift kink instability (Büchner & Kuska 1999; Yoon & Lui 2001; Silin & Büchner 2003). Hereafter, we call it the relativistic drift sausage instability (RDSI). Its eigen profiles at $k\lambda = 0.25$ are presented in Figure 21. The anti-symmetric profile of δB_x and the symmetric profile of δD_+ are consistent with its sausage-type structure. The RDSI is usually faster than the RDKI in a very long wavelength limit of $k\lambda \ll 1$. On the other hand, the fastest RDKI is usually faster than the RDSI. In our runs, we could not observe any sign of the RDSI. This result is consistent with P96, who suggested that Landau damping stabilizes the (nonrelativistic) drift sausage instability.

4.5. Particle acceleration

In this section, we discuss the particle acceleration in the nonlinear stage, based on our previous works (Zenitani & Hoshino 2005a). To study the acceleration site, we select

high-energy positrons whose y -positions (y) and kinetic energies (ε) at $t/\tau_c = 82.0$ satisfy the conditions $6.4 \leq y/\lambda < 12.8$ and $\varepsilon/mc^2 > 20$. Their spatial distributions and energy spectrum at three stages (light gray at $t/\tau_c = 46.0$, gray at $t/\tau_c = 64.0$, and dark gray at $t/\tau_c = 82.0$) are presented in Figure 22. The selected positrons are accelerated in an “acceleration channel” (AC) around $z \sim 0$ into the $+x$ direction. Inside the AC, positive E_y regions are in a row (e.g. middle left panel in Fig. 15), and then high-energy particles successively skip across the multiple positive E_y regions along the AC, once their Larmor radii are comparable with or larger than the quarter wavelength of the RDKI. In energy spectra at $t/\tau_c = 46$ and 64 in Figure 14, particle acceleration effect is only observed in the high-energy range of $\varepsilon \gtrsim 10 - 12mc^2$, where the gyro radius ($r_L = \gamma(c/\omega_c) \gtrsim (1.5 - 2)\lambda$) exceeds the quarter wavelength $\pi/(2k_y) \sim 1.6\lambda$. This threshold condition $\gamma c/\omega_c \gtrsim \pi/(2k_y)$ yields

$$\varepsilon \gtrsim \pi e B_0 \lambda / (2k_y \lambda) = \pi T / (\beta k_y \lambda) \sim \pi T / \beta. \quad (31)$$

So, the particle acceleration in the AC will smear out in the thick current sheet of $\beta \ll 1$, because only a few particles satisfy this criterion.

The folded structure evolves into the mixed stage when its z -displacement (Δz) is nearly the same as the half-wavelength of the RDKI ($\Delta z \sim \pi/k_y \sim \pi\lambda$). So, in Zenitani & Hoshino (2005a), we evaluated the timescale of the nonlinear stage (τ_N) as

$$\tau_N \sim \pi \lambda / \bar{v}_z \sim (\pi/\beta) \tau_c, \quad (32)$$

where we assume that the typical z -displacement speed $\bar{v}_z \sim (0.2 - 0.3)c$ is approximated by the typical counter-streaming speed of βc . After that, a lot of low-energy particles in the current sheet start to interact with the electric fields. The magnetic energy consumption is well explained by Joule heating between the average electric field \bar{E}_y and the zeroth order current $\bar{J}_y \sim cB_0/(4\pi\Delta z)$ in the broadened current sheet. We also approximated the dissipation timescale (τ_D) considering the energy consumption rate:

$$\tau_D \sim (2\Delta z B_0^2 / 8\pi) (2\Delta z \bar{E}_y \bar{J}_y)^{-1} \sim (\pi/\beta) \tau_c, \quad (33)$$

where $\bar{E}_y \sim (1/2)(\bar{v}_z/c)B_0$ and where the factor of $(1/2)$ represents that the electric field is not uniform around the AC. From equations (11), (12), (32), and (33), we estimate the maximum energy gain during the nonlinear stage and the mixed stage,

$$\Delta\varepsilon_{est} \sim ec\bar{E}_y(\tau_N + \tau_D) \sim eB_0\pi\lambda \sim 2\pi T/\beta. \quad (34)$$

Typical estimated values $\varepsilon_{est} = \varepsilon_{max0} + \Delta\varepsilon_{est}$ are presented in Table 3.

4.6. Case studies

We have further carried out simulation runs with various temperatures, runs D1-D5 ($T/mc^2 = 16, 4, 1, 1/4$, and $1/16$) in Table 3. We observe current sheet modulation and the electromagnetic perturbations by the RDKI in all five cases. Relativistic runs ($T/mc^2 \gtrsim 1$) show similar results in many aspects of energy spectra, wavelength, and growth rates. The energy spectra in runs D1 and D2 have both the hot thermal component and the nonthermal component and they look “proportional” to those in run D3. The wavelength and the growth rates are nearly the same, when normalized by the sheet thickness or the light transit time. In less relativistic runs ($T/mc^2 < 1$), we observe longer wavelength modes (mode 2; $k_y\lambda = 0.49$) as predicted by the theory (eq. [27]). A high-energy tail becomes less apparent (Figure 23*b*) and the RDKI grows slower than the theory (eq. [26]). This is probably because the fluid theory loses validity in the nonrelativistic limit (eq. [16]).

Figure 23*a* shows enhancements of the particle kinetic energies or the released magnetic energy in runs D1-D5 with $T/mc^2 = 16, 4, 1, 1/4, 1/16$. Energies are normalized by the pressure energy in the original current sheet. The saturation level always seems to be 5 – 6, and the timescale for the energy release is $t \sim 20\tau_c$. Nonrelativistic cases take more time due to their slower growth rates. Comparing with reconnection cases in Figure 12*a*, the amount of released energy is comparable; however, due to its faster growth rates their timescales are shorter in the relativistic regime. Figure 23*b* presents the nonthermal ratio parameter of K_{nth}/K . We could not resolve the nonthermal part with our method in run D5 ($T/mc^2 = 1/16$) and in the late-thermalized stage of run D4 ($T/mc^2 = 1/4$). The parameter seems to become small as a smaller T is used and the particle acceleration is enhanced in the relativistic regime of $T/mc^2 \gtrsim 1$. Comparing Figures 12*b* and 23*b*, apparently reconnection produces more nonthermal energy than the RDKI. Although the width of the simulation box is not the same ($25.6\lambda[y]$ for the RDKI, $102.4\lambda[x]$ for reconnection), the RDKI’s nonthermal ratio will not change. If we look at the smaller region around the X -type region, we will obtain a higher nonthermal ratio. Remember the partial spectrum at $t/\tau_c = 100.0$ in Figure 3. Apparently, the partial spectra is highly dominated by nonthermal energy and it is integrated over $-12.8 < x/\lambda < 12.8$ — the same width as the RDKI simulation domains (25.6λ). So, as an origin of the nonthermal particles, reconnection is a more favorable candidate due to the acceleration processes around the X -type region. On the contrary, the RDKI quickly converts magnetic energy into plasma thermal energy or plasma heat.

The maximum energies (ε_{max}) obtained by the RDKI are presented in Table 3. They are compared with our estimate from equation (34), which seems to be a good approximation for these runs with $\beta = 0.3$. This relation will not be valid in the “thick” current sheet with small β . In thicker current sheets, the Larmor radius becomes smaller compared with the

wavelength, so that particle acceleration may not take place. The maximum energies (ε_{max}) obtained by reconnection are also presented in Table 3. As far as we have investigated, maximum energies by reconnection are far larger than those by the RDKI, and reconnection is undoubtedly favorable to accelerate high-energy particles. By the way, we do not know the upper limit energy of acceleration by the single reconnection. In Table 3, we roughly estimate the maximum energy by $\varepsilon_{est} = eE_y c(L_x/2c) = eB_0 L_x/2$ considering that the acceleration electric field E_y is on the same order as B_0 and considering that reconnection continues until two outflow jets toward the $\pm x$ -directions meet each other at the periodic boundary at $x = \pm L_x/2$.

5. Discussions

5.1. Parameter dependence and comparison

Figure 24 shows theoretical and observed growth rates of simulation runs R1-R5 and D1-D5 with different temperature parameters $T/mc^2 = 1/16, 1/4, 1, 4, 16$. The growth rates (ω_i) are normalized by the light transit time τ_c . The linear growth rates of magnetic reconnection are calculated from the reconnected field energy $\sum B_z^2$ in the neutral plane. The normalized growth rates are around $\tau_c \omega_i \sim 0.03$. Theoretical growth rates of reconnection are represented by the theory of the relativistic tearing mode (Zelenyi & Krasnoselskikh 1979). Its growth rates γ_{RTI} in pair plasmas are:

$$\tau_c \gamma_{RTI} = \begin{cases} \frac{1}{\sqrt{\pi}} k\lambda(1 - k^2\lambda^2)\beta^{3/2} (2T/\gamma_\beta mc^2)^{-1/2} & (T \ll mc^2) \\ \frac{2\sqrt{2}}{\pi} k\lambda(1 - k^2\lambda^2)\beta^{3/2} & (T \gg mc^2) \end{cases} \quad (35)$$

In the relativistic case, we obtain the maximum growth rate by setting $k\lambda = 1/\sqrt{3}$

$$\tau_c \gamma_{RTI} \lesssim 0.35\beta^{3/2}, \quad (36)$$

For $\beta = 0.3$, the maximum growth rate is $\tau_c \gamma_{RTI} \sim 0.055$. This rate is 1.7 – 2.0 times faster than simulation results, but remember that reconnection is not identical to the tearing mode. The linear growth rates of RDKI/DKI are obtained from the perturbed magnetic field δB_x in the neutral plane, and the growth rates of the most dominant mode are selected. The growth rates of the RDKI/RDSI are estimated by equations (26) and (29). The growth rate of the DKI increases as T increases in the nonrelativistic regime of $T/mc^2 \ll 1$. On the contrary, the RDKI is insensitive to T . The theory (eq. [26]) clearly explains this signature. Relativistic pressure enhances effective inertia through the fluid enthalpy term, and then the enhanced inertia cancels further growth of the RDKI. So, the rate stays constant in the

relativistic limit. Since equation (27) slightly exceeds unity ($k_y\lambda \sim 1.1 - 1.3$) in relativistic cases of $T \gtrsim mc^2$, another criteria of equation (29) is presented as a second branch of the theoretical rate in Figure 24. Both criteria give $\tau_c\gamma_{RDKI} \sim 0.19$, which limits the obtained value of $\tau_c\omega_i \sim 0.11$.

Figure 25 shows eigen and theoretical growth rates as functions of the current sheet thickness $\beta = \lambda_D/\lambda$ (eq. [14]). In this case, the plasma temperature is fixed to $T = mc^2$. The upper limit of the RDKI β (eq. [30]), the upper limit of the relativistic tearing mode $0.35\beta^{3/2}$ (eq. [35]), eigen growth rates for the relativistic tearing mode, and eigen growth rates for the RDKI are presented. For eigen growth rates for the RDKI, we present two cases with $k\lambda = 0.5$ and $k\lambda = 1.0$ because we do not know what wavelength is the most dominant and because the DKI theories use the long-wavelength assumption ($k\lambda \lesssim 1$). In the range of $0.03 < k\lambda < 0.7$, it seems that the eigen growth rates of the RTI and the RDKI/RDSI are well limited by their theoretical upper limit. It is still unclear how the instabilities grow in the thick current sheet and whether or not they are limited by the upper limits. This should be investigated by larger PIC simulations or relativistic two-fluid MHD simulations. Theoretically, equation (28) makes sense as an upper limit of the RDKI, because β also represents the current (eq. [12]) and because the RDKI is a current-driven instability.

Figure 26 compares the theoretical growth rates as functions of two parameters: T/mc^2 and β . We use equations (26), (29), and (35). Generally, the RDKI/RDSI grows faster than reconnection. Most parts of the frontmost flat region ($\beta \ll 1$ and $T \gg mc^2$) rely on equation (28) or (29). It seems that the RDKI's rate goes down around $\beta \sim 1$, but our fluid theory is no longer valid here, because the current sheet is too thin (eq. [14]). Also, the fluid theory is not valid around the backward region of $\beta > 0.1$ and $T/mc^2 \ll 1$, where the Larmor radius is comparable with or larger than the sheet thickness λ (eq. [16]). Except for these invalid regions, we can conclude that the RDKI is more likely to occur in a relativistic hot condition of $T/mc^2 \gtrsim 1$.

Importantly, in the relativistic regime of $T \gtrsim mc^2$ our simulations show no drastic change. The various aspects are similar: the evolution of the reconnection or the RDKI structure, time history of total energy, nonthermal ratio, relative height of the nonthermal slope, and the maximum energy of the nonthermal tail. These results are quite reasonable considering the following facts. The characteristic speed is around the light speed $\sim c$ (Table 1) and the typical Larmor radius relative to the sheet width is nearly constant (eq. [15]). It is straightforward that the typical gyro period ($\Omega_c^{-1} = \gamma/\omega_c$) is constant when normalized by the light transit time $\tau_c = \lambda/c$. So, we can conclude that the physical processes are “similar” in these relativistic cases, as long as we consider kinetics. Therefore, by employing the moderately-relativistic simulation ($T \approx mc^2$), we may figure out ultra-relativistic kinetic

evolution, which is computationally more expensive; one has to resolve the gyro motion of the lowest energy particle (ω_c^{-1}) while the system evolution is governed by the typical gyro period ($\Omega_c^{-1} = \gamma/\omega_c$). If we start to consider radiation effects, we need another approach because the synchrotron radiation highly depends on the ultra relativistic Lorentz factor: γ or T/mc^2 .

5.2. Pulsar wind problem

Let us discuss a possible application to the striped pulsar wind (Lyubarsky & Kirk 2001; Kirk & Skjæraasen 2003). Our comparison shows that the RDKI is the most likely process in the current sheet, as long as plasmas are relativistic hot ($T \gtrsim mc^2$). If the current-aligned magnetic field (the so-called guide field, B_y) exists, secondary magnetic reconnection will dominate (Zenitani & Hoshino 2005b); however, magnetic fields are expected to be highly toroidal inside the striped pulsar wind due to the fast rotation of the neutron star, and therefore the guide field would be weak or unlikely to exist. Therefore, here we assume that the RDKI dominates in the striped current sheets.

Kirk & Skjæraasen (2003) (hereafter KS03) has examined the magnetic dissipation problem by using the expanding current sheets model. They estimated the magnetic dissipation rate, assuming that striped current sheets are expanding with a “dissipation speed” of $c\beta_c$, where β_c is the dimensionless speed. They assumed magnetic reconnection as the most likely process, and they estimated the dissipation speed with the growth rate of the relativistic tearing mode (Zelenyi & Krasnoselskikh 1979) in their “tearing mode-limited” scenario. Importantly, one-dimensional simulation results are well described by an asymptotic analytic solution in all cases. From the flux-freezing equation (eq. [38] in KS03), the entropy equation (eq. [39] in KS03) and the dissipation speed (β_c), the asymptotic solution $\Delta \propto (r/r_L)^{-q}$ can be obtained, where Δ is a ratio of the current sheet thickness to the wavelength of the striped current sheets and q is the spectral index. Two of their scenarios are presented in Table 2. They assume that the current sheets are completely dissipated at the radial distance of r_{max}/r_{LC} from the central neutron star, where r_{LC} is the distance of the light cylinder. Two columns of r_{max}/r_{LC} are presented; the first column is the analytical form, and the second column is the estimated value by using Crab parameters. The termination shock is at $r/r_{LC} = 2.0 \times 10^9$, and so $r_{max}/r_{LC} < 2.0 \times 10^9$ is a favorable result. The “fast” scenario is a physical upper limit; its dissipation speed is based on the relativistic sound speed of $c/\sqrt{3}$. In the tearing mode-limited scenario, they set $c\beta_c = \lambda\gamma_{RTI}$, where $\tau_c\gamma_{RTI} = \beta^{3/2}$ (eq. [35] in KS03) is a simplified form of equation (35). If we modify the dissipation speed with the maximum growth rate of $\tau_c\gamma_{RTI} \sim 0.35\beta^{3/2}$ (from eq. [36]), the dissipation distance (r_{max})

increases by 50%. The modified value is presented as the “tearing mode–limited (modified)” scenario in Table 2.

We propose a similar dissipation scenario by the RDKI. We consider that the current sheet evolves to the broadened current sheet by the RDKI and then it continues to expand by the cascading RDKI processes. We call it the “drift kink mode–limited” scenario. We assume that the current sheet expands by $h \sim (3-4)$ times by single RDKI process: the sheet’s typical width λ becomes $\lambda' \sim h\lambda$, where the prime denotes the physical value in the broadened current sheet after the first instability is saturated. Consequently, the plasma density in the current sheet is $n'_0 \sim n_0/h$. For simplicity, we ignore the particle acceleration effect, because nonthermal particles carry less than 10% of kinetic energies (in Fig. 23*b*). Assuming the pressure balance condition $2n_0T = 2n'_0T' = B_0^2/8\pi$, the second-stage plasma temperature increases to $T' \sim hT$ due to the nonlinear mixing of the RDKI. Then, the Debye length $(\lambda'_D/\lambda') \sim (\lambda_D/\lambda)$ and the Larmor radius $(r'_L/\lambda') \sim (r_L/\lambda)$ remain constant, relative to the sheet width. Regarding the relativistic Harris parameters, $\beta' \sim \beta$ remains constant, while the temperature increases, $T' \sim hT$. According to Figure 26, the RDKI is likely to occur again in the broadened condition. So, it is quite plausible that the current sheet is dissipated by series of the RDKI processes. Topologically, the RDKI is favorable for the current sheet dissipation scenario, because it does evolve into the broadened current sheet structure, while it is not sure that reconnection evolves into the broaden current sheet. In thick current sheets of $\beta \ll 1$, we evaluate the dissipation speed using equation (30); $c\beta_c \sim \lambda\gamma_{RDKI} = c\beta$. It is a good approximation of the eigen growth rates by a factor of 1-3 (Fig. 25). Using this, following KS03’s method, one can obtain the asymptotic index $q = 2/5$ and relevant values. These values are presented in Table 2. If we use the typical parameters, the obtained dissipation distance is $r_{max}/r_L = 3.1 \times 10^9$. This value is 3 times better than the original tearing mode scenario and the drift-kink-mode scenario substantially improves the dissipation model in the striped pulsar wind.

By the way, our DKI/RDKI theory is based on a long-wavelength assumption. In a nonrelativistic ion-electron plasma, it is reported that short-wavelength current sheet instability grows faster than long-wavelength modes (Suzuki et al. 2002). Magnetic dissipation becomes even faster, if short-wavelength mode grows faster in a thick current sheet. In a thin current sheet, the nonthermal accelerations are more likely to transfer magnetic energy into the y -momentum $\pm p_y$ of nonthermal plasmas. Then, since the z -pressure relatively decreases, the current sheet may be thinner and the RDKI may grow faster (Fig. 26). In a thick current sheet of $\beta \ll 1$, we can probably ignore nonthermal acceleration because few particles satisfy the threshold condition (eq. [31]). When neighboring current sheets come close to each other, they start to collide each other during the nonlinear stage of the RDKI. We compare several runs with different simulation box size L_z (runs D3, D3b, and

D3c in Table 3). In run D3c, the current sheets collide with each other across the periodic z -boundaries and more than 90% of the magnetic energy is dissipated into particle energy. On the other hand, the actual dissipation speed may be somewhat slower than the growth rates of the instabilities (both the RDKI and the tearing mode). So, an effective dissipation speed should be further investigated by a larger simulation, in which we can observe cascading evolution of the RDKI. If the current sheet structure survives at the termination shock, the magnetic fields may further be dissipated by the collision of the shock and current sheets. In the downstream of the shock, magnetic reconnection may be triggered by turbulent electric fields.

In summary, we propose the RDKI as an alternative magnetic dissipation scenario in the striped current sheets, based on our theoretical estimates. At present we do not know whether or not the RDKI is the final key to explain the σ problem; however, the drift kink mode scenario is obviously more favorable than the reconnection/tearing mode scenario.

5.3. Miscellaneous discussions

In ion-electron reconnection, various instabilities occur in different scales. For example, the LHDI occurs on an electron scale, the DKI on an ion scale, reconnection is on a macroscopic MHD scale, and then coupling across these scales leads a complexity of plasma phenomena. In this study, we investigate a very thin current sheet in e^\pm plasmas. Consequently, both the reconnection and the RDKI occur in the same scale as the current sheet. Both of them greatly violate the current sheet structure, and we discuss them as competing processes. When we consider a “thick” current sheet, the RDKI or other cross-field instabilities may occur on a rather microscopic scale, and then they may interact with the macroscopic reconnection process. These situations should be further investigated.

It has been believed that the reconnection’s global energy dissipation is controlled by the Hall physics (Birn et al. 2001). In pair plasmas, the relevant positron’s contribution is canceled out by electron’s, and so the Hall effect does not exist. However, simulations of pair plasma reconnection (Zenitani & Hoshino 2001; Jaroschek et al. 2004; Zenitani & Hoshino 2005b; Bessho & Bhattacharjee 2005) reported fast reconnection rates [v_{in}/v_{out} or $E_y/(cB_0)$, $E_y/(v_A B_0)$] of 0.1 or above. This issue is equivalent to the question “What is the origin of the reconnection electric field?”. In classical nonrelativistic studies, the electric field is described by

$$\mathbf{E} = -\mathbf{v}_e \times \mathbf{B} - \frac{1}{n_e e} \nabla \cdot \Pi_e - \frac{m_e}{e} \left(\frac{\partial \mathbf{v}_e}{\partial t} + \mathbf{v}_e \cdot \nabla \mathbf{v}_e \right), \quad (37)$$

where v_e is the electron’s velocity and Π_e is the electron’s pressure tensor. The Hall effect

comes from the difference in the electron Lorentz term ($\mathbf{v}_e \times \mathbf{B}$) and its ion counterpart, and it smears out in the case of pair plasmas. Bessho & Bhattacharjee (2005) showed that the pressure-tensor term explains the electric field in the vicinity of the neutral region. Similar analysis can be applied to relativistic cases, using the relativistic pressure tensor (Write & Hadley 1975). In addition, the electron’s inertia may be of importance due to the increasing mass from the Lorentz effect.

5.4. Summary and Conclusion

Let us summarize and conclude this paper. We have carried out series of PIC simulations of relativistic current sheet problems in pair plasmas. We examine the relativistic magnetic reconnection and we report that particles can be accelerated near the magnetic pile-up region as well as the X -type region. We have also studied the current sheet instabilities, which exists in the perpendicular plane to reconnection. The parameter survey shows that properties of these two processes are similar in the relativistic regime of $T \gtrsim mc^2$, as long as we consider the kinetics. In addition, by comparing their growth rates, the RDKI is the more likely process in the relativistic regime of $T \gtrsim mc^2$. Therefore we propose that the magnetic dissipation in the striped pulsar wind should be re-considered by using the RDKI.

The authors are grateful to T. Terasawa, S. Abe, I. Shinohara, T. Yokoyama, S. Shibata, K. Nagata, C. Jaroschek, and M. Hesse for fruitful discussions. This work was supported by the facilitates of JAXA and the Solar-Terrestrial Environment Laboratory, Nagoya University. One of the authors (S. Z.) was granted a fellowship from the Japan Society of the Promotion of Science and GEST program of University of Maryland Baltimore County. S. Z. is grateful to the editor and anonymous referee for improving the original manuscript.

REFERENCES

- J. Arons 1979, Space Sci. Rev., 24, 437
- N. Bessho and A. Bhattacharjee 2005, Phys. Rev. Lett., 95, 245001
- E. G. Blackman and G. B. Field 1994, Phys. Rev. Lett., 72, 494
- J. Birn, M. F. Thomsen, J. E. Borovsky, G. D. Reeves, D. J. McComas, R. D. Belian and M. Hesse 1997, J. Geophys. Res., 102, 2325

- J. Birn, J. F. Drake, M. A. Shay, B. N. Rogers, R. E. Denton, M. Hesse, M. Kuznetsova, Z. W. Ma, A. Bhattacharjee, A. Otto and P. L. Pritchett 2001, *J. Geophys. Res.*, 106, 3715
- J. Büchner and J. P. Kuska 1999, *Annales Geophysicae*, 17, 604
- F. V. Coroniti 1990, *ApJ*, 349, 538
- W. Daughton 1998, *J. Geophys. Res.*, 103, 29429
- W. Daughton 1999, *J. Geophys. Res.*, 104, 28701
- R. C. Davidson et al. 1977, *Phys. Fluids*, 20, 301
- T. di Matteo 1998, *MNRAS*, 299, L15
- G. Drenkhahn and H. C. Spruit 2002, *A&A*, 391, 1141
- J. W. Dungey 1961, *Phys. Rev. Lett.*, 6, 47
- C. H. Jaroschek, R. A. Treumann, H. Lesch and M. Scholer 2004, *Phys. Plasmas*, 11, 1151
- E. G. Harris 1962, *Nuovo Cimento*, 23, 115
- J. Heyvaerts, C. Norman and R. E. Pudritz 1988, *ApJ*, 330, 718
- R. Horiuchi and T. Sato 1999, *Phys. Plasmas*, 6, 4565
- M. Hoshino, T. Mukai, T. Terasawa and I. Shinohara 2001, *J. Geophys. Res.*, 106, 25979
- J. D. Huba and J. F. Drake 1981, *Physics of Fluids*, 24, 1650
- C. F. Kennel and F. V. Coroniti 1984, *ApJ*, 283, 694
- J. G. Kirk and O. Skjæraasen 2003, *ApJ*, 591, 366
- S. S. Komissarov, M. Barkov and M. Lyutikov 2006, *MNRAS*, 374, 415
- N. A. Krall and P. C. Liewer 1971, *Phys. Rev. A*, 4, 2094
- D. A. Larrabee, R. V. E. Lovelace and M. M. Romanova 2003, *ApJ*, 586, 72
- H. Lesch and G. T. Birk 1998, *ApJ*, 499, 167
- Y. Lyubarsky and J. G. Kirk 2001, *ApJ*, 547, 437
- Y. Lyubarsky 2005, *A&A*, 358, 113

- M. Lyutikov and D. Uzdensky 2003, *ApJ*, 589, 893
- M. Lyutikov 2003, *MNRAS*, 346, 540
- F. C. Michel 1982, *Reviews of Modern Physics*, 54, 1
- F. C. Michel 1994, *ApJ*, 431, 397
- E. N. Parker 1957, *J. Geophys. Res.*, 62, 509
- T. D. Phan, J. T. Gosling, M. S. Davis and R. M. Skoug 2006, *Nature*, 439, 175
- P. L. Pritchett, F. V. Coroniti and V. K. Decyk 1996, *J. Geophys. Res.*, 101, 27413
- M. M. Romanova and R. V. E. Larrabee 1992, *A&A*, 262, 26
- C. T. Russell, K. K. Khurana, D. E. Huddleston and M. G. Kivelson 1998, *Science*, 280, 1061
- S. Saito and J. Sakai 2006, *ApJ*, 652, 793
- J. Sakai and T. Kawata 1980, *Physical Society of Japan Journal*, 49, 747
- R. Schopper, H. Lesch and G. T. Birk 1998, *A&A*, 335, 26
- I. Shinohara and M. Fujimoto 2005, *Frontiers of Magnetospheric Physics, COSPAR Colloquia Series 16*, 123.
- I. Shinohara, H. Suzuki, M. Fujimoto and M. Hoshino 2001, *Phys. Rev. Lett.*, 8709, 5001
- I. Silin and J. Büchner 2003, *Physics of Plasmas*, 10, 3561
- T. W. Speiser 1965, *J. Geophys. Res.*, 70, 4219
- H. Suzuki, M. Fujimoto and I. Shinohara 2002, *Advances in Space Research*, 30, 2663
- Synge, J. L. 1957, "The Relativistic Gas", Interscience Publishers Inc.
- K. G. Tanaka, I. Shinohara and M. Fujimoto 2006, *J. Geophys. Res.*, 111, 11
- N. Watanabe and T. Yokoyama 2006, *ApJ*, 647, L123
- T. P. Wright and G. R. Hadley 1975, *Phys. Rev. A*, 12, 686
- P. H. Yoon and J. F. Drake 1996, *J. Geophys. Res.*, 101, 27327
- P. H. Yoon and A. T. Y. Lui 2001, *J. Geophys. Res.*, 106, 1939

- L. M. Zelenyi and V. V. Krasnoselskikh 1979, *Astronomicheskii Zhurnal*, 56, 819
- S. Zenitani and M. Hoshino 2001, *ApJ*, 562, L63
- S. Zenitani and M. Hoshino 2003, *Proceedings of the 28th International Cosmic Ray Conference*, p.2043
- S. Zenitani and M. Hoshino 2005a, *ApJ*, 618, L111
- S. Zenitani and M. Hoshino 2005b, *Phys. Rev. Lett.*, 95, 095001
- Z. Zhu and R. M. Winglee 1996, *J. Geophys. Res.*, 101, 4885

A. Nonthermal ratio parameter

In this appendix, we describe our “nonthermal ratio” index, to discuss the nonthermal acceleration. By integrating over half of the simulation box, we obtain the plasma energy spectra $F_{sim}(\varepsilon)$. The total particle number N and the total kinetic energy K satisfy

$$N = \int_0^\infty d\varepsilon F_{sim}(\varepsilon) \quad (A1)$$

$$K = \int_0^\infty d\varepsilon F_{sim}(\varepsilon)(\varepsilon - mc^2). \quad (A2)$$

Next, we consider an ideal thermal gas, which is described by the Jüttner-Synge distribution with unknown temperature T . Similarly, we consider the particle number N_{gas} , the total kinetic energy K_{gas} and its energy spectra $F_{gas}(\varepsilon)$ for this ideal gas. The Jüttner-Synge gas has the relation (Synge 1957)

$$K_{gas}/(N_{gas}mc^2) = 3(T/mc^2) + [K_1(mc^2/T)/K_2(mc^2/T) - 1], \quad (A3)$$

where $K_{1,2}(x)$ is the modified Bessel function of the second kind. Then, we assume that $N_{gas} = N$ and $K_{gas} = K$, so that F_{gas} represents an “equivalent” thermal distribution. Since equation (A3) is a monotonically increasing function of (T/mc^2) , we can find a unique solution of $T = T'$. Then, we calculate the nonthermal parameter by comparing the original spectrum $F_{sim}(\varepsilon)$ and the equivalent thermal spectrum $F_{gas}(\varepsilon)$ with $T = T'$. The relation between the two spectra is illustrated in Figure 27; the spectrum F_{gas} is presented in light gray, and the spectrum F_{sim} is presented behind it in white and dark gray. The two spectra cross at several points, e.g. $\varepsilon = \varepsilon_1, \varepsilon_2, \dots$, and we define the nonthermal energy K_{nth} as

$$K_{nth} = \int_{\varepsilon_2}^\infty [F_{sim}(\varepsilon) - F_{gas}(\varepsilon)](\varepsilon - mc^2) d\varepsilon, \quad (A4)$$

where F_{sim} exceeds F_{gas} at $\varepsilon = \varepsilon_2$ in the highest energy tail. This “nonthermal” part is presented in dark gray in Figure 27. We use the ratio of the kinetic energy carried by this tail (K_{nth}) to the total kinetic energy (K) as the nonthermal ratio parameter.

B. Linear analysis of relativistic drift kink/tearing mode

We start with the relativistic fluid equation of motion,

$$T_{(fluid)}^{\alpha\beta} = (\varepsilon + p)u^\alpha u^\beta + p\eta^{\alpha\beta} \quad (B1)$$

where $T_{(fluid)}$ is the energy-momentum tensor for fluid, ε is the energy, p is the pressure, u is the mean four-velocity of the fluid, and $\eta^{\alpha\beta}$ is the metric tensor. In order to preserve the energy and the momentum in the system,

$$\frac{\partial}{\partial x^\beta}(T_{(fluid)}^{\alpha\beta} + T_{(EM)}^{\alpha\beta}) = 0 \quad (B2)$$

should be satisfied, where $T_{(EM)}$ is the electromagnetic stress-energy tensor. Using the relation

$$\frac{\partial}{\partial x^\beta} T_{(EM)}^{\alpha\beta} = -F^{\alpha\beta} j_\beta, \quad (B3)$$

where F is the electro-magnetic tensor and j is the four current, equation B2 can be modified to

$$\frac{\partial}{\partial x^\beta} T_{(fluid)}^{\alpha\beta} = F^{\alpha\beta} j_\beta. \quad (B4)$$

The spatial three components of equation (B4) can be described (See Sakai & Kawata (1980)) as

$$\frac{\gamma_s^2}{c^2}(p_s + \varepsilon_s)\left(\frac{\partial}{\partial t} + \mathbf{v}_s \cdot \nabla\right)\mathbf{v}_s = -\nabla p_s + \gamma_s q_s n_s \left(\mathbf{E} + \frac{\mathbf{v}_s}{c} \times \mathbf{B}\right) - \frac{\mathbf{v}_s}{c^2}(\gamma_s q_s n_s \mathbf{E} \cdot \mathbf{v}_s + \frac{\partial p_s}{\partial t}), \quad (B5)$$

where the subscript s denotes the species. p for positrons and e for electrons. We also use the particle conservation law,

$$\frac{\partial}{\partial t}(\gamma_s n_s) + \nabla \cdot (\gamma_s n_s \mathbf{v}_s) = 0, \quad (B6)$$

and Maxwell equations,

$$\nabla \times \mathbf{B} = \frac{4\pi}{c} \sum_s \gamma_s q_s n_s \mathbf{v}_s + \frac{1}{c} \frac{\partial \mathbf{E}}{\partial t} \quad (B7)$$

$$\nabla \times \mathbf{E} = -\frac{1}{c} \frac{\partial \mathbf{B}}{\partial t} \quad (B8)$$

We assume the plasma is an adiabatic gas,

$$p_s \propto n_s^\Gamma. \quad (B9)$$

where Γ is the polytropic index of $\Gamma = 4/3$. Then, we replace some variables in equations (B5), (B6), (B7) and (B8) by using

$$\varepsilon_s = n_s m_0 c^2 + \frac{1}{\Gamma - 1} p_s \quad (B10)$$

$$\gamma_s = [1 - (\mathbf{v}_s/c)^2]^{-1/2} \quad (B11)$$

$$d_s = \gamma_s n_s \quad (B12)$$

where d_s stands for the number density in the observed frame.

Finally, equations (B5), (B6), (B7), (B8) and (B9) are linearized for the the Harris field model, assuming that perturbations are given by $\delta f \propto \delta f(z) \exp(ik_x x + ik_y y + \omega_i t)$. The operators are transformed as $\partial/\partial x \rightarrow ik_x$ and $\partial/\partial y \rightarrow ik_y$, and we normalize the first-order perturbations as $\mathbf{B} = B_0(F(z)\hat{x} + b_y\hat{y}) + B_0\hat{\mathbf{b}}$, $\mathbf{E} = B_0\hat{\mathbf{e}}$, $\mathbf{v}_s = \pm c\beta + c\beta\hat{\mathbf{v}}_s$, $d_s = d_{s0}f(z) + d_{s0}\hat{d}_s$, and $p_s = p_{s0}f(z) + p_{s0}\hat{p}_s$, where $F(z) = \tanh(z/\lambda)$ and $f(z) = \cosh^{-2}(z/\lambda)$. The parameter $b_y = B_y/B_0$, the amplitude of the guide field, is set to 0. For numerical simplicity, some physical properties are calculated in the form of summaries or differences between the positron values and electron values, $\hat{D}_\pm = \hat{d}_p \pm \hat{d}_e$, $\hat{P}_\pm = \hat{p}_p \pm \hat{p}_e$, and $\hat{\mathbf{V}}_\pm = \hat{\mathbf{v}}_p \pm \hat{\mathbf{v}}_e$. We have

$$\frac{\partial}{\partial t}\hat{b}_x = -ck_y(i\hat{e}_z) + c\frac{\partial}{\partial z}\hat{e}_y \quad (\text{B13})$$

$$\frac{\partial}{\partial t}\hat{b}_y = -c\frac{\partial}{\partial z}\hat{e}_x + ck_x(i\hat{e}_z) \quad (\text{B14})$$

$$\frac{\partial}{\partial t}(i\hat{b}_z) = ck_x\hat{e}_y - ck_y\hat{e}_x \quad (\text{B15})$$

$$\frac{\partial}{\partial t}\hat{e}_x = -A_1f(z)\hat{V}_{x-} + ck_y(i\hat{b}_z) - c\frac{\partial}{\partial z}\hat{b}_y \quad (\text{B16})$$

$$\frac{\partial}{\partial t}\hat{e}_y = -A_1(\hat{D}_+ + f(z)\hat{V}_{y-}) + c\frac{\partial}{\partial z}\hat{b}_x - ck_x(i\hat{b}_z) \quad (\text{B17})$$

$$\frac{\partial}{\partial t}(i\hat{e}_z) = -A_1f(z)(i\hat{V}_{z-}) + ck_y\hat{b}_x - ck_x\hat{b}_y \quad (\text{B18})$$

$$\begin{aligned} \frac{\partial}{\partial t}\hat{D}_+ &= -c\beta k_y(i\hat{D}_-) - c\beta f(z)\left(k_x(i\hat{V}_{x+}) + k_y(i\hat{V}_{y+}) + \frac{\partial}{\partial z}\hat{V}_{z+}\right) \\ &\quad - c\beta f'(z)\hat{V}_{z+} \end{aligned} \quad (\text{B19})$$

$$\begin{aligned} \frac{\partial}{\partial t}(i\hat{D}_-) &= c\beta k_y\hat{D}_+ + c\beta f(z)\left(k_x\hat{V}_{x-} + k_y\hat{V}_{y-} - \frac{\partial}{\partial z}(i\hat{V}_{z-})\right) \\ &\quad - c\beta f'(z)(i\hat{V}_{z-}) \end{aligned} \quad (\text{B20})$$

$$\frac{\partial}{\partial t}\hat{P}_+ = \Gamma\frac{\partial}{\partial t}\hat{D}_+ - \Gamma\frac{\beta^2}{1-\beta^2}\frac{\partial}{\partial t}\hat{V}_{y-} \quad (\text{B21})$$

$$\frac{\partial}{\partial t}(i\hat{P}_-) = \Gamma\frac{\partial}{\partial t}(i\hat{D}_-) - \Gamma\frac{\beta^2}{1-\beta^2}\frac{\partial}{\partial t}(i\hat{V}_{y+}) \quad (\text{B22})$$

$$\frac{\partial}{\partial t}(i\hat{V}_{x+}) = c\beta k_y\hat{V}_{x-} + k_x\frac{A_2}{f(z)}\hat{P}_+ + 2A_3(i\hat{b}_z) - A_3b_y(i\hat{V}_{z-}) \quad (\text{B23})$$

$$\frac{\partial}{\partial t}\hat{V}_{x-} = -c\beta k_y(i\hat{V}_{x+}) - k_x\frac{A_2}{f(z)}(i\hat{P}_-) + (2A_3/\beta)\hat{e}_x - A_3b_y\hat{V}_{z+} \quad (\text{B24})$$

$$\frac{\partial}{\partial t}(i\hat{V}_{y+}) + \frac{A_2\beta}{c}\frac{\partial}{\partial t}(i\hat{P}_-) = c\beta k_y \hat{V}_{y-} + k_y \frac{A_2}{f(z)} \hat{P}_+ + A_3 F(z)(i\hat{V}_{z-}) \quad (\text{B25})$$

$$\begin{aligned} \frac{\partial}{\partial t}\hat{V}_{y-} + \frac{A_2\beta}{c}\frac{\partial}{\partial t}\hat{P}_+ &= -c\beta k_y(i\hat{V}_{y+}) - k_y \frac{A_2}{f(z)}(i\hat{P}_-) + 2A_3(\beta^{-1} - \beta)\hat{e}_y \\ &\quad + A_3 F(z)\hat{V}_{z+} \end{aligned} \quad (\text{B26})$$

$$\begin{aligned} \frac{\partial}{\partial t}\hat{V}_{z+} &= -c\beta k_y(i\hat{V}_{z-}) - \frac{A_2}{f(z)}\frac{\partial}{\partial z}\hat{P}_+ - \frac{A_3 F(z)}{f(z)}\hat{D}_+ \\ &\quad - 2A_3\hat{b}_x + A_3 b_y \hat{V}_{x-} - A_3 F(z)\hat{V}_{y-} \end{aligned} \quad (\text{B27})$$

$$\begin{aligned} \frac{\partial}{\partial t}(i\hat{V}_{z-}) &= c\beta k_y \hat{V}_{z+} - \frac{A_2}{f(z)}\frac{\partial}{\partial z}(i\hat{P}_-) - \frac{A_3 F(z)}{f(z)}(i\hat{D}_-) \\ &\quad + (2A_3/\beta)(i\hat{e}_z) + A_3 b_y(i\hat{V}_{x+}) - A_3 F(z)(i\hat{V}_{y+}) \end{aligned} \quad (\text{B28})$$

where $f'(z) = (\partial/\partial z)f(z) = -(2/\lambda)\tanh(z/\lambda)\cosh^{-2}(z/\lambda)$, $A_1 = 4\pi e c \beta d_0/B_0$, $A_2 = (p_0/c\beta)[(\gamma_\beta^2/c^2)(n_0 m c^2 + [\Gamma/(\Gamma-1)]p_0)]^{-1}$, and $A_3 = (e d_0 B_0/c)[(\gamma_\beta^2/c^2)(n_0 m c^2 + [\Gamma/(\Gamma-1)]p_0)]^{-1}$. Note that equations (B21), (B22), (B25) and (B26) still contain time derivative terms. We reorganize the six equations (B19), (B20), (B21), (B22), (B25), and (B26) to obtain $(\partial/\partial t)\hat{P}_+$, $(\partial/\partial t)(i\hat{P}_-)$, $(\partial/\partial t)(i\hat{V}_{y+})$, and $(\partial/\partial t)\hat{V}_{y-}$.

$$\begin{pmatrix} \frac{\partial}{\partial t}\hat{P}_+ \\ \frac{\partial}{\partial t}\hat{V}_{y-} \end{pmatrix} = \frac{\Gamma}{1 - \Gamma A_3 \beta^3 \gamma_\beta^2 / c} \begin{pmatrix} 1 & -f(z)\beta^2 \gamma_\beta^2 \\ -A_3 \beta / [c f(z)] & 1/\Gamma \end{pmatrix} \begin{pmatrix} \text{rhs of (B19)} \\ \text{rhs of (B26)} \end{pmatrix} \quad (\text{B29})$$

$$\begin{pmatrix} \frac{\partial}{\partial t}\hat{P}_- \\ \frac{\partial}{\partial t}\hat{V}_{y+} \end{pmatrix} = \frac{\Gamma}{1 - \Gamma A_3 \beta^3 \gamma_\beta^2 / c} \begin{pmatrix} 1 & -f(z)\beta^2 \gamma_\beta^2 \\ -A_3 \beta / [c f(z)] & 1/\Gamma \end{pmatrix} \begin{pmatrix} \text{rhs of (B20)} \\ \text{rhs of (B25)} \end{pmatrix} \quad (\text{B30})$$

Finally, after replacing $\partial/\partial t \rightarrow \omega_i$, all the above relations can be solved as an eigen value problem of the following matrix. Solving this problem, we obtain the growth rate of the instability ω_i and the z -structure of the perturbations for given k_x and k_y . The matrix is

$$\omega_i \begin{pmatrix} \hat{b}_x \\ \hat{b}_y \\ i\hat{b}_z \\ \hat{e}_x \\ \hat{e}_y \\ i\hat{e}_z \\ \hat{D}_+ \\ i\hat{D}_- \\ \hat{P}_+ \\ i\hat{P}_- \\ i\hat{V}_{x+} \\ \hat{V}_{x-} \\ i\hat{V}_{y+} \\ \hat{V}_{y-} \\ \hat{V}_{z+} \\ i\hat{V}_{z-} \end{pmatrix} = \begin{pmatrix} a_{11} & a_{12} & \dots & \dots & a_{1n} \\ a_{21} & a_{22} & & & a_{2n} \\ & & & & \\ & & & & \\ \vdots & & \ddots & & \vdots \\ & & & & \\ a_{n1} & a_{n2} & \dots & \dots & a_{nn} \end{pmatrix} \begin{pmatrix} \hat{b}_x \\ \hat{b}_y \\ i\hat{b}_z \\ \hat{e}_x \\ \hat{e}_y \\ i\hat{e}_z \\ \hat{D}_+ \\ i\hat{D}_- \\ \hat{P}_+ \\ i\hat{P}_- \\ i\hat{V}_{x+} \\ \hat{V}_{x-} \\ i\hat{V}_{y+} \\ \hat{V}_{y-} \\ \hat{V}_{z+} \\ i\hat{V}_{z-} \end{pmatrix}. \quad (\text{B31})$$

We set 241 grids in the z -direction and 20 grids per λ ; therefore, we solve $-6\lambda \leq z \leq 6\lambda$. The size of the matrix is 3856^2 . The conductive-wall conditions are assumed at the boundaries. For selected cases, we use 361 grids in z , 5776^2 grids per a matrix and we checked the effect of the grid resolution and the boundary positions. In the case of $\beta = 0.3$, the grid number shows an error less than 1%. In the case of $\beta < 0.1$, we have to choose a high resolution configuration with 5776^2 grids. For numerical stability, we sometimes add a small amplitude of the (nonrelativistic) viscosity term to the fluid equation. The equivalent Reynolds number (R_e) is set to $R_e = \rho_0 \lambda c \beta / \mu = 10^6 - 10^7$. The eigen modes for the tearing mode or the RDKI/RDSI mode are usually obtained without this viscosity term. We need a small amplitude of the viscosity term to solve short-wavelength RDKI modes ($k_x = 0, k_y \gtrsim 1$) and the oblique modes ($k_x \neq 0, k_y \neq 0$).

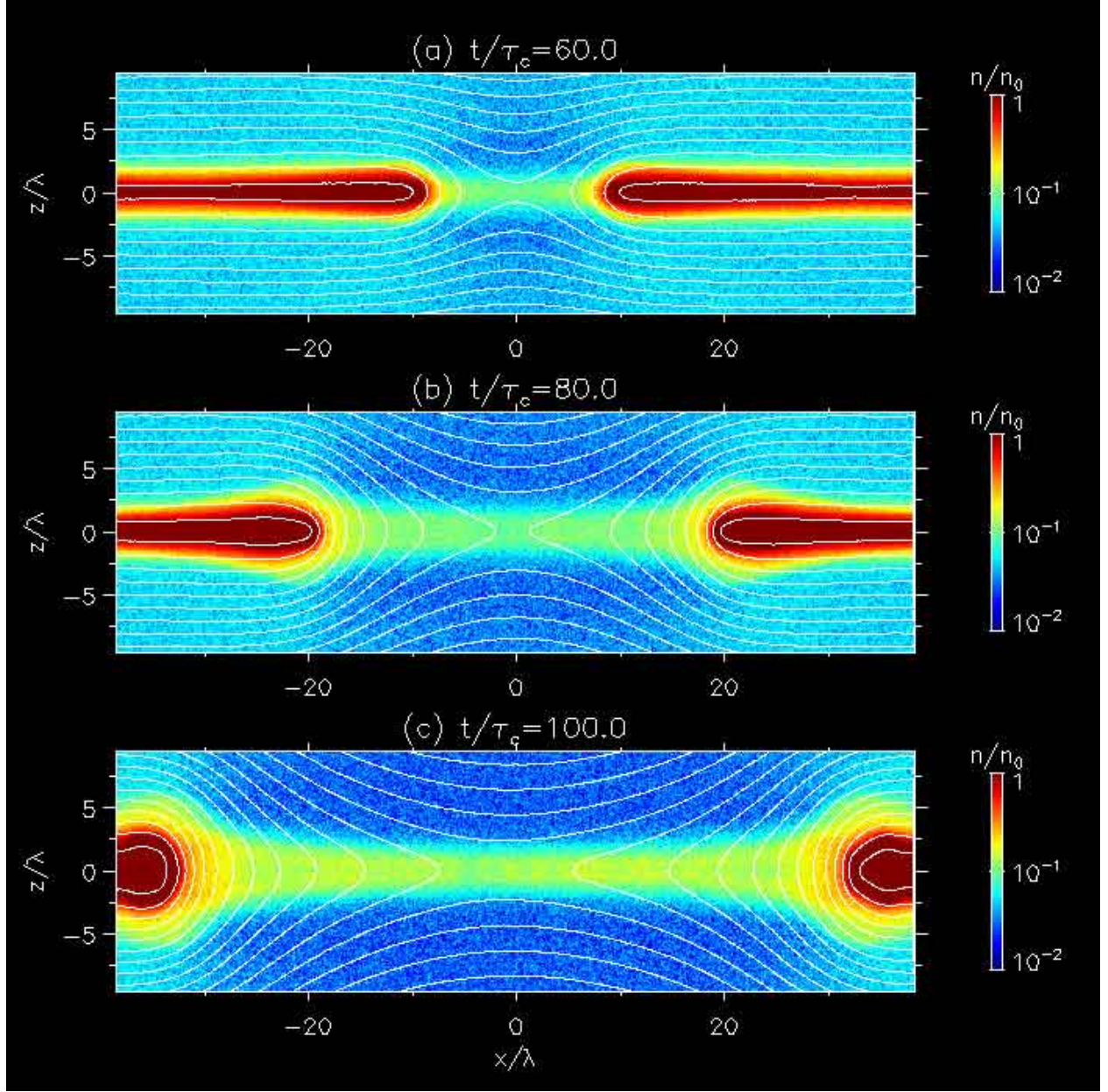


Fig. 1.— Snapshots of relativistic reconnection at typical stages: $t/\tau_c = 60.0, 80.0$, and 100.0 . In the left panels, the solid lines represent magnetic field lines and the color contour shows the density of plasmas normalized by the original plasma sheet density $\rho_0 = 2\gamma_\beta n_0$.

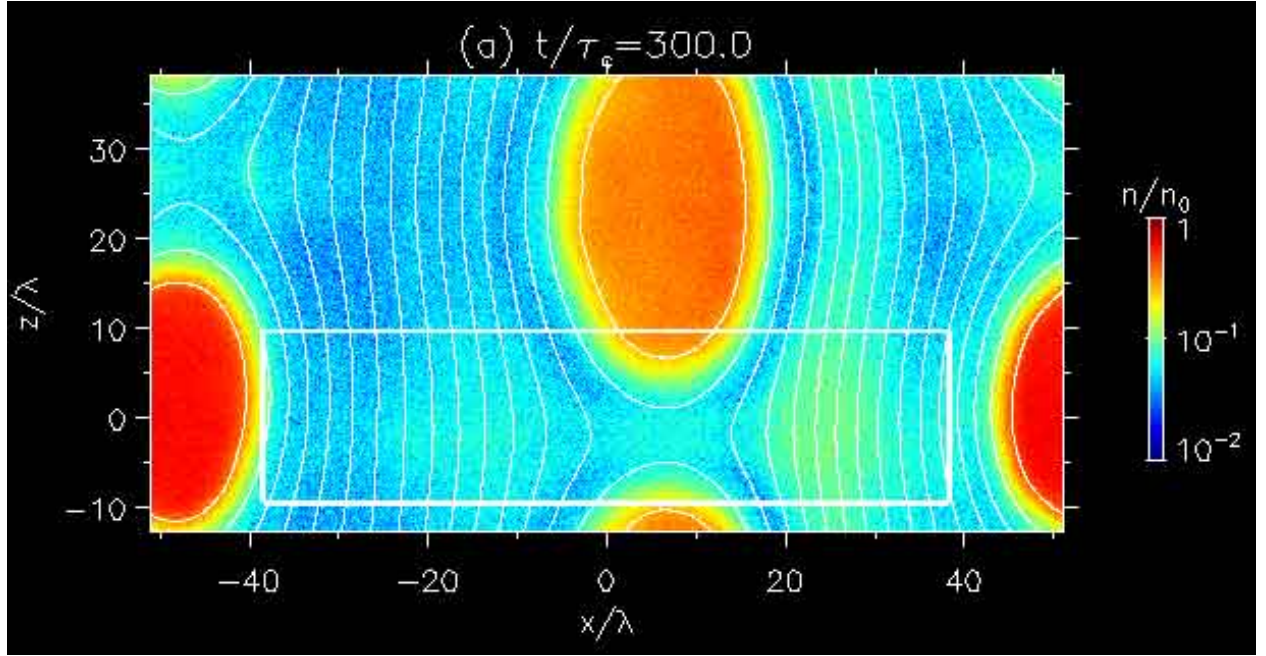


Fig. 2.— Late-time snapshot at $t/\tau_e = 300.0$ of run R3. Main ($-12.8 < z/\lambda < 12.8$) and sub ($12.8 < z/\lambda < 38.4$) simulation boxes are presented. The white rectangle shows the region of interest in Fig. 1.

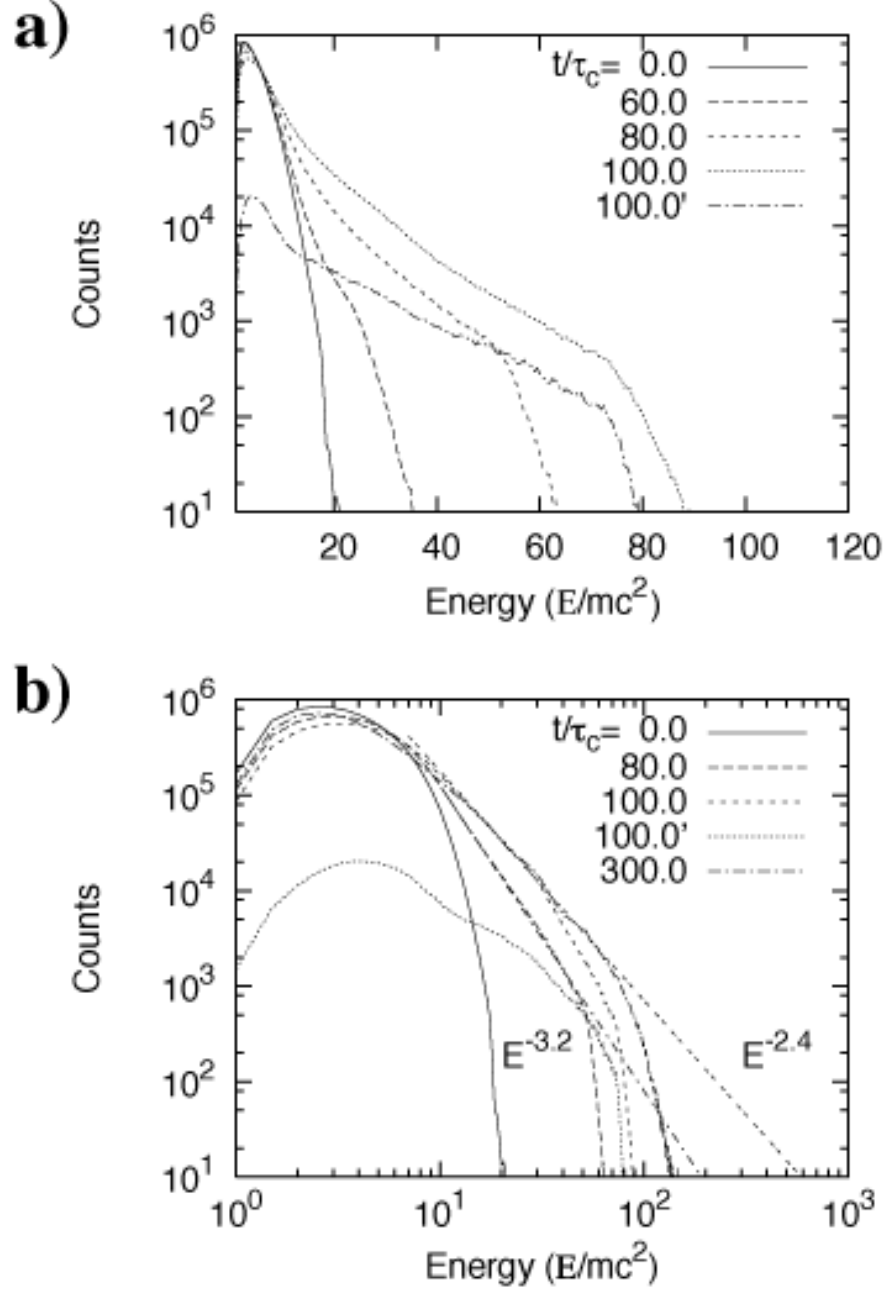


Fig. 3.— Particle energy spectra in run R3 are presented in log-linear and log-log format. The partial energy spectra at $t/\tau_c = 100.0$ is also presented as $t/\tau_c = 100.0'$.

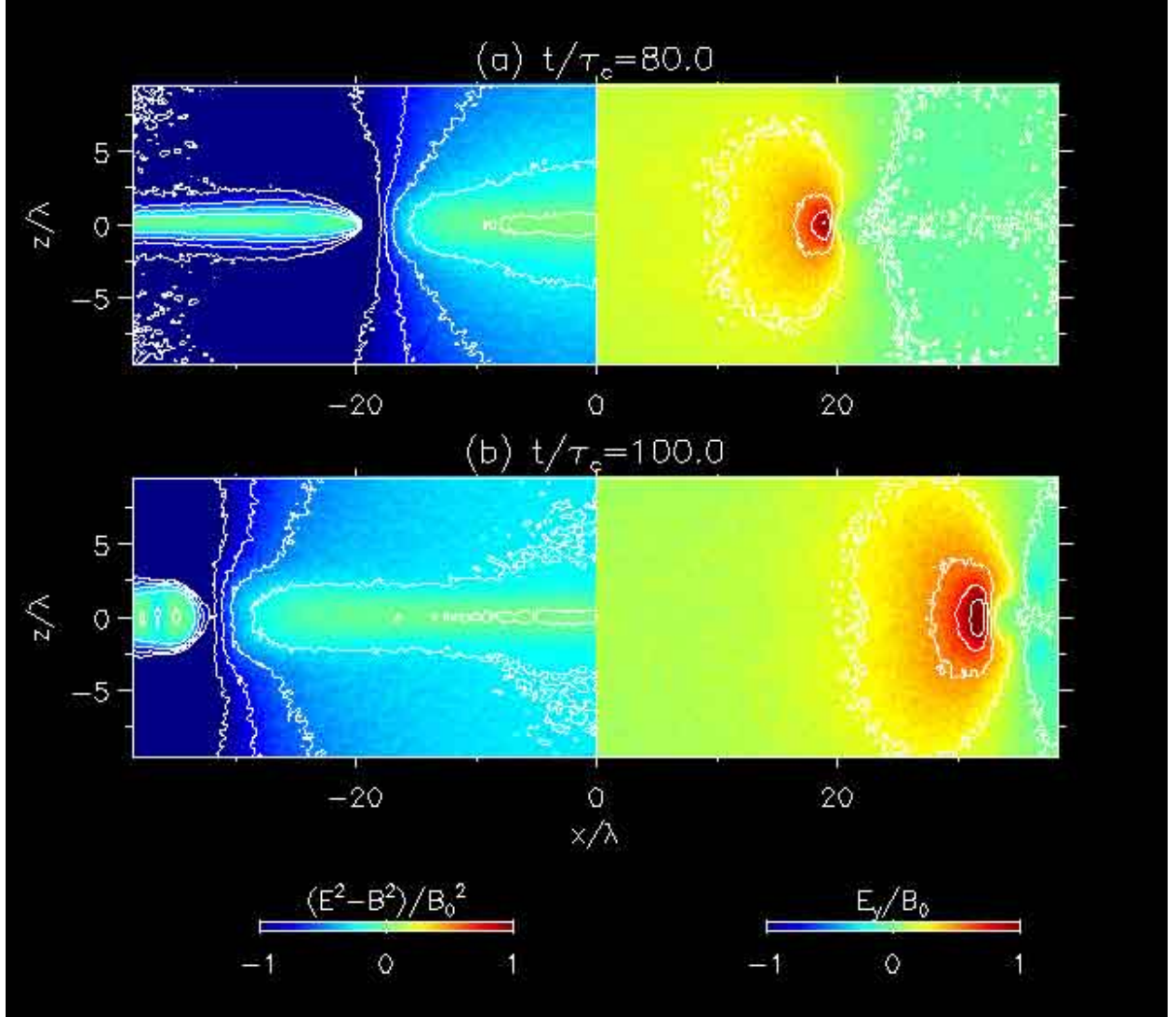


Fig. 4.— Structure of the electric field in run R3. The left half displays the Lorentz invariant $E^2 - B^2$, normalized by B_0^2 . The right half displays the reconnection electric field E_y , normalized by B_0 .

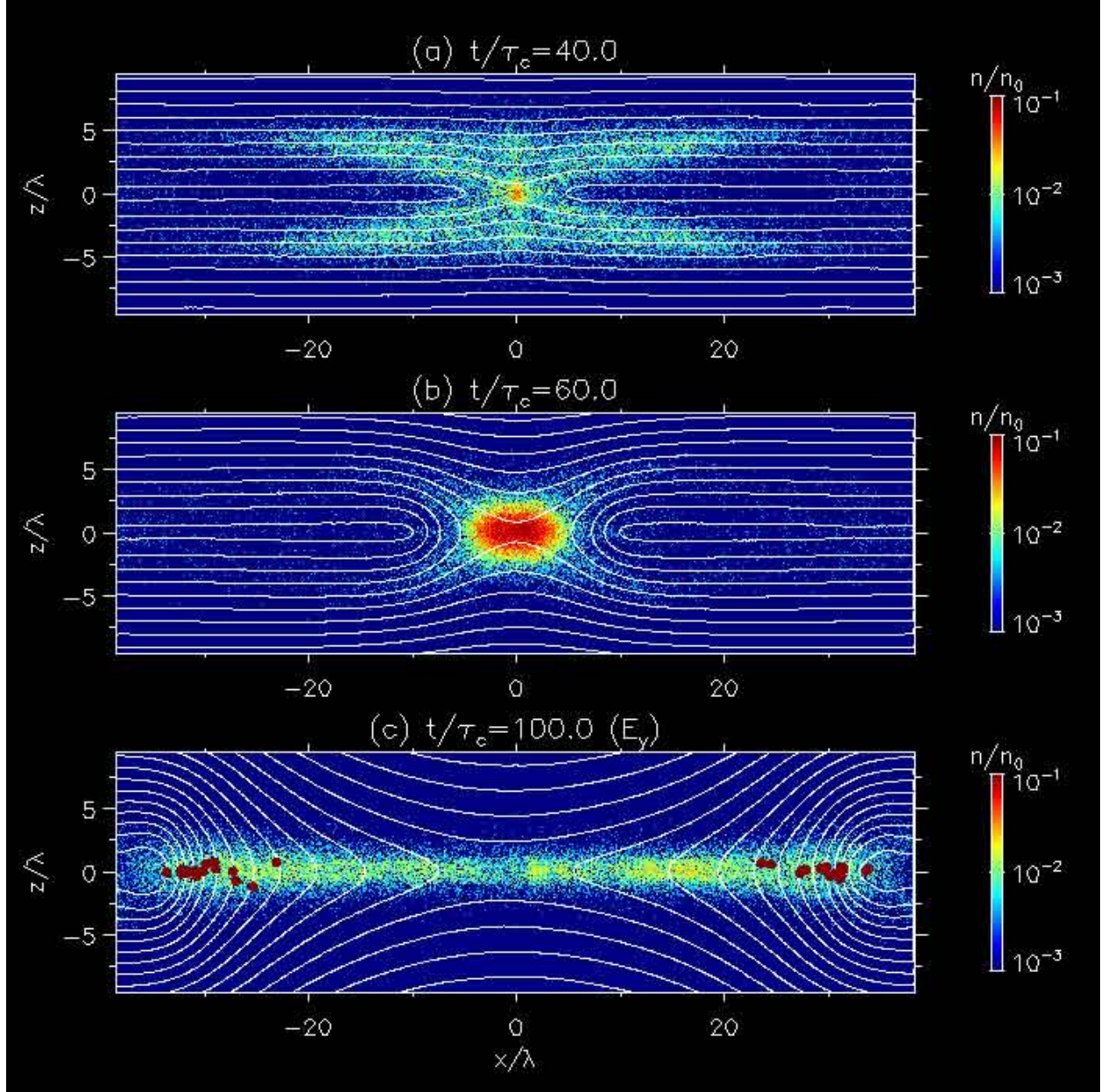


Fig. 5.— Spatial distributions of accelerated particles whose energy exceeds $50mc^2$ at $t/\tau_c = 100.0$. White lines show magnetic field lines. The red marks in the bottom panel show the spatial distribution of highly accelerated particles, whose energy exceeds $90mc^2$.

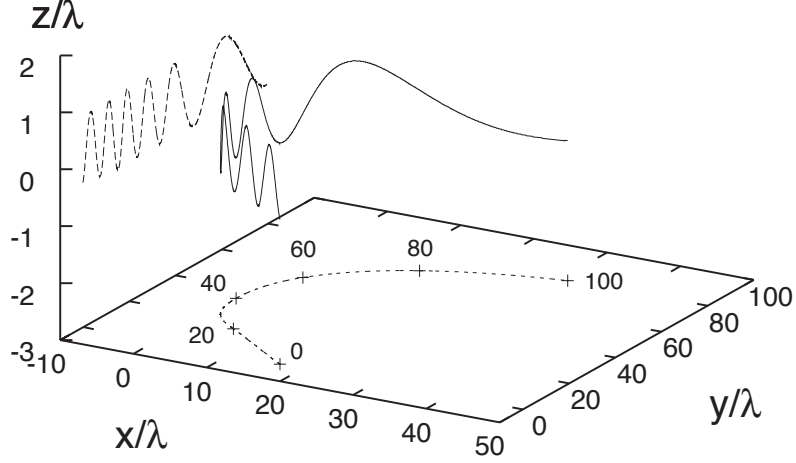


Fig. 6.— Particle trajectory (*solid line*) of a highly accelerated positron, its xz - and xy -projections (*dashed lines*) are presented. Labels in the xy plane show the relevant times.

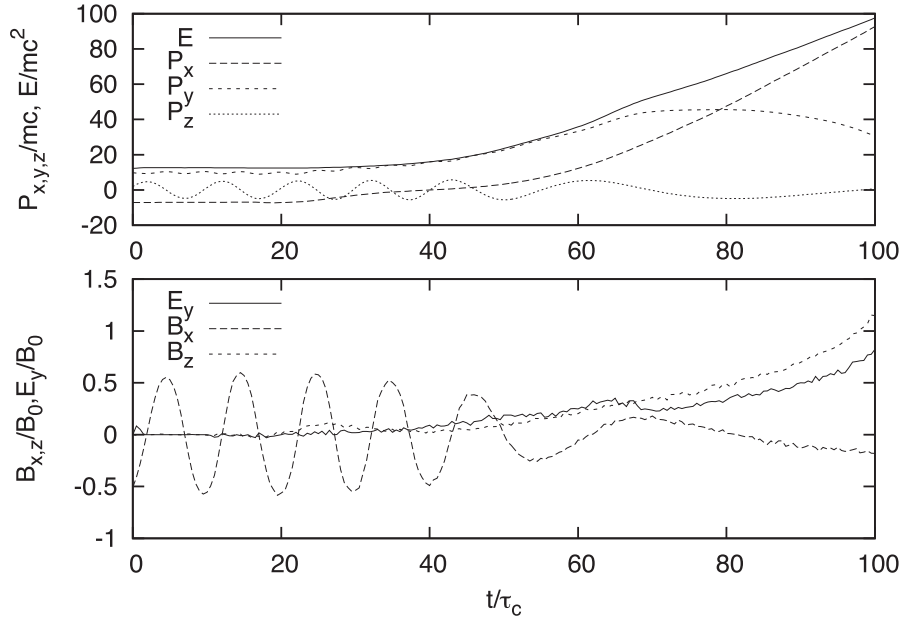


Fig. 7.— Time history of the particle's energy, momentum and the electromagnetic field at the positron's position in the simulation frame.

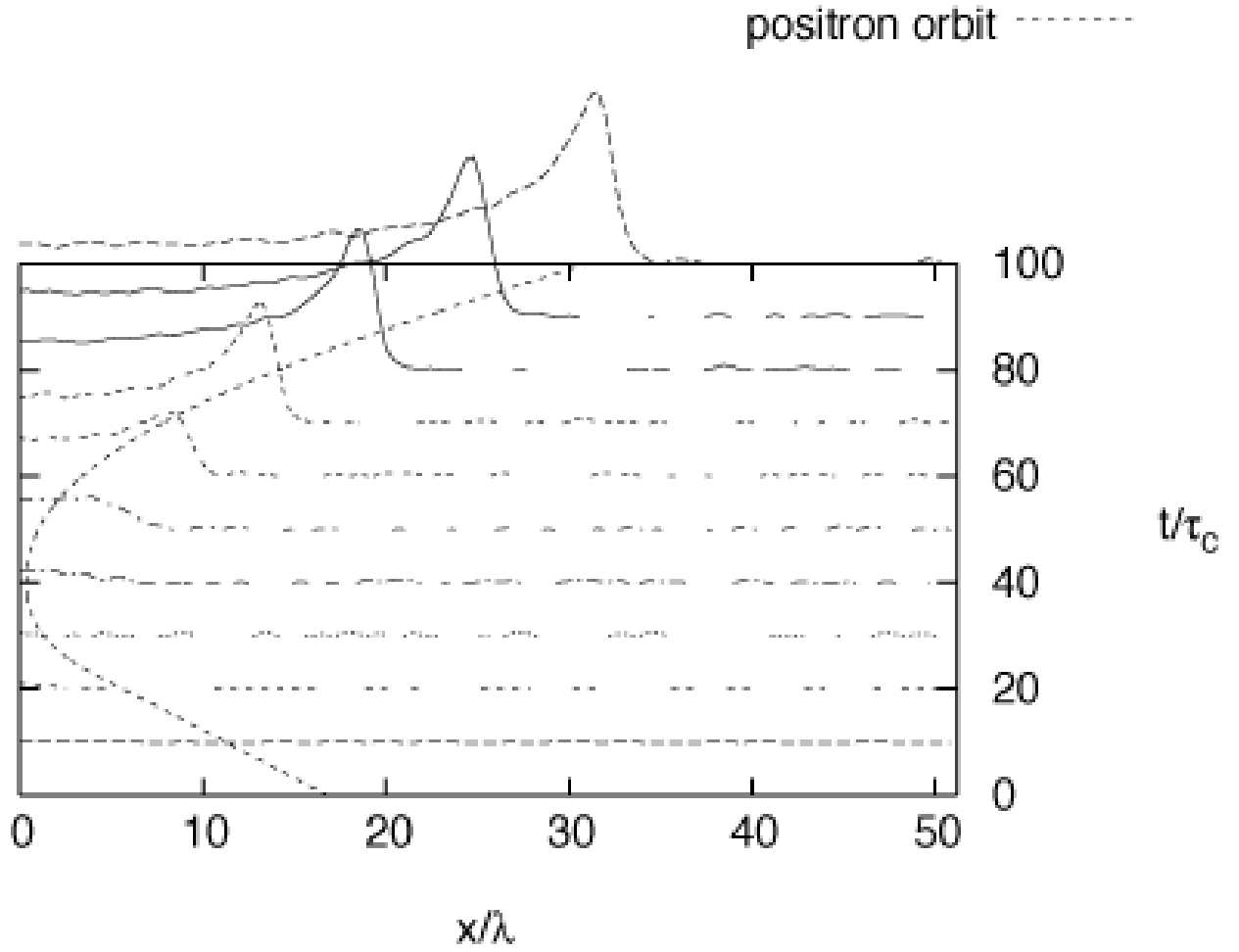


Fig. 8.— x - t diagram of the positron trajectory and the reconnection electric field E_y along the neutral sheet ($z = 0$).

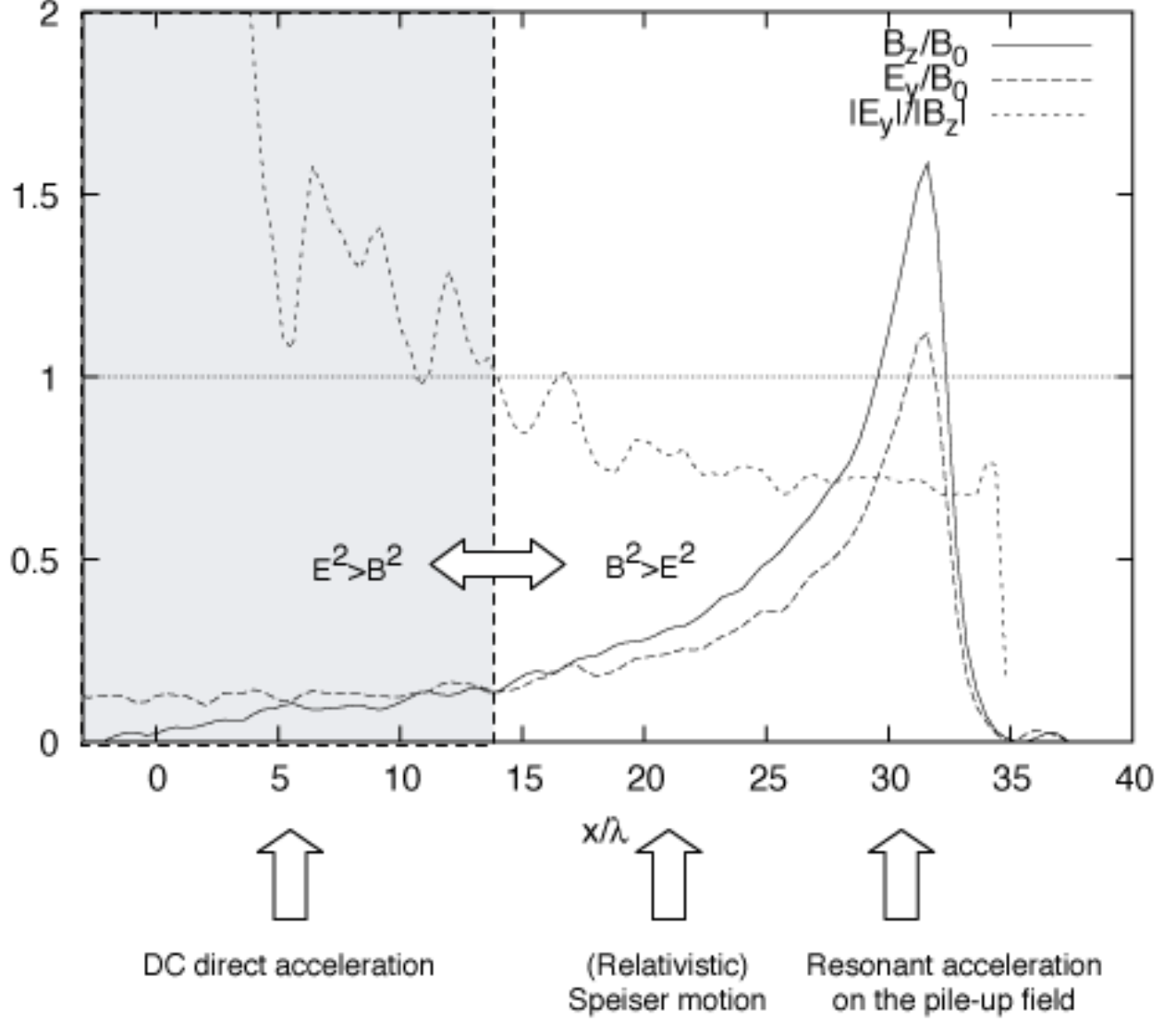


Fig. 9.— Field structure in the neutral sheet at $t/\tau_c = 100.0$. The normalized electromagnetic fields B_z and E_y and the ratio of $|E_y|/|B_z|$ are presented.

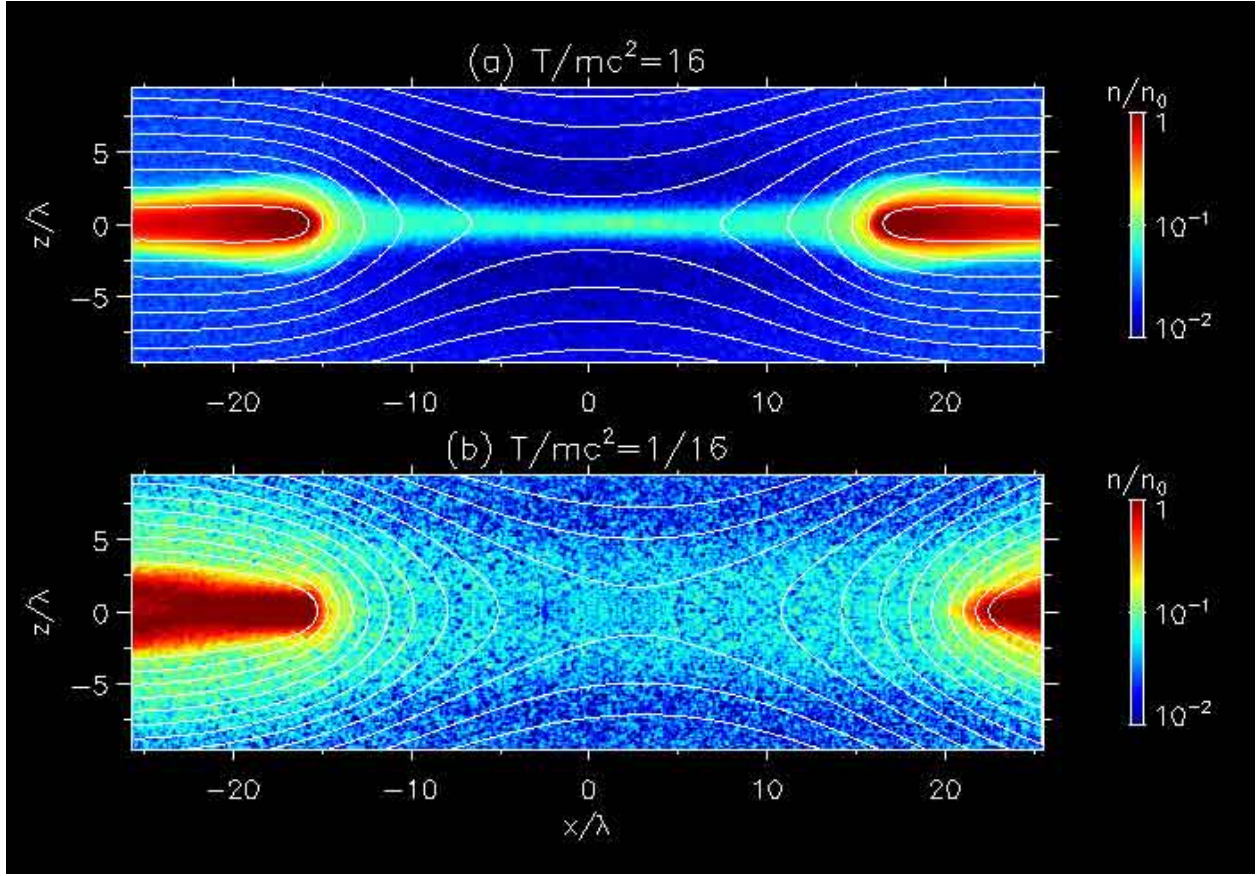


Fig. 10.— Snapshots of runs for $T/mc^2 = 16$ (*top*) and $T/mc^2 = 1/16$ (*bottom*).

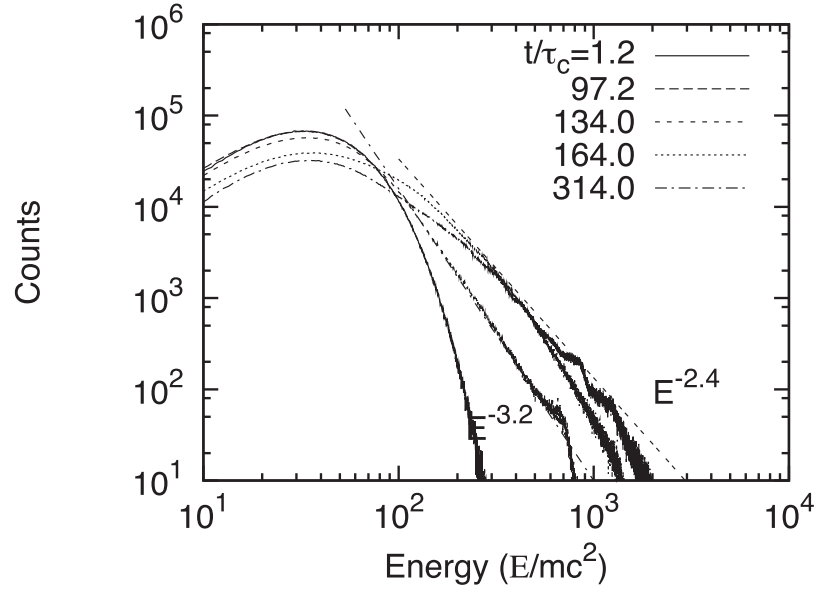


Fig. 11.— Particle energy spectra in run R1 in log-log format.

Run	T/mc^2	v_{in_max}/c	v_{out_max}/c	V_A/c	V_A^{inflow}/c
R1	16	0.6	0.97	0.57	0.99
R2	4	0.4	0.9	0.57	0.99
R3	1	0.39	0.88	0.53	0.98
R4	1/4	0.29	0.63	0.45	0.94
R5	1/16	0.19	0.53	0.30	0.84

Table 1: Maximum outflow velocity compared with two types of the Alfvén velocity: (1) the typical Alfvén velocity and (2) the inflow Alfvén velocity.

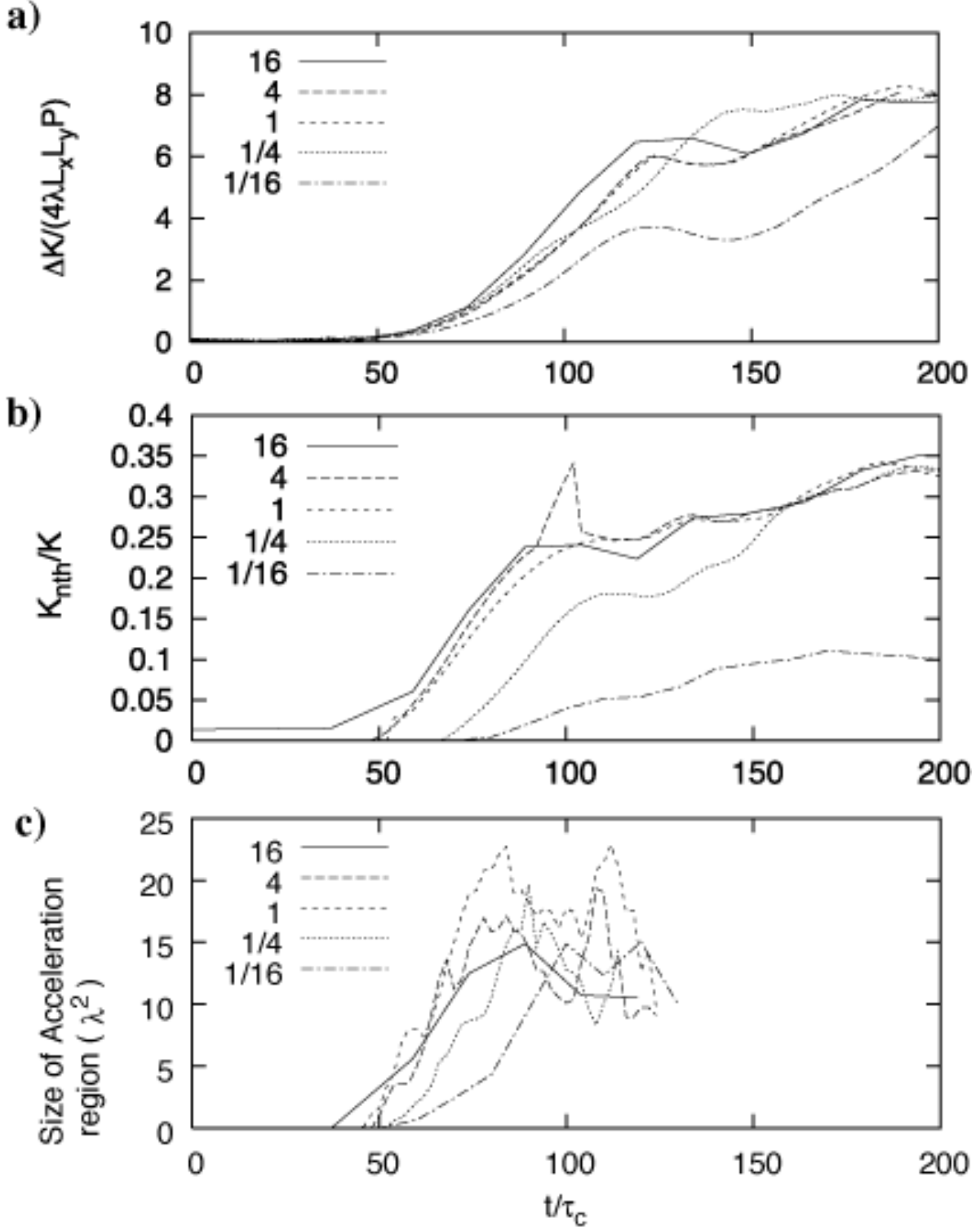


Fig. 12.— (a) Enhancements of the particle kinetic energies in the reconnection runs with $T/mc^2 = 16, 4, 1, 1/4, 1/16$. Energies and time are normalized by the pressure in the original current sheet and the light transit time, respectively. (b) Nonthermal ratio parameters for reconnection. (c) Size of the acceleration region.

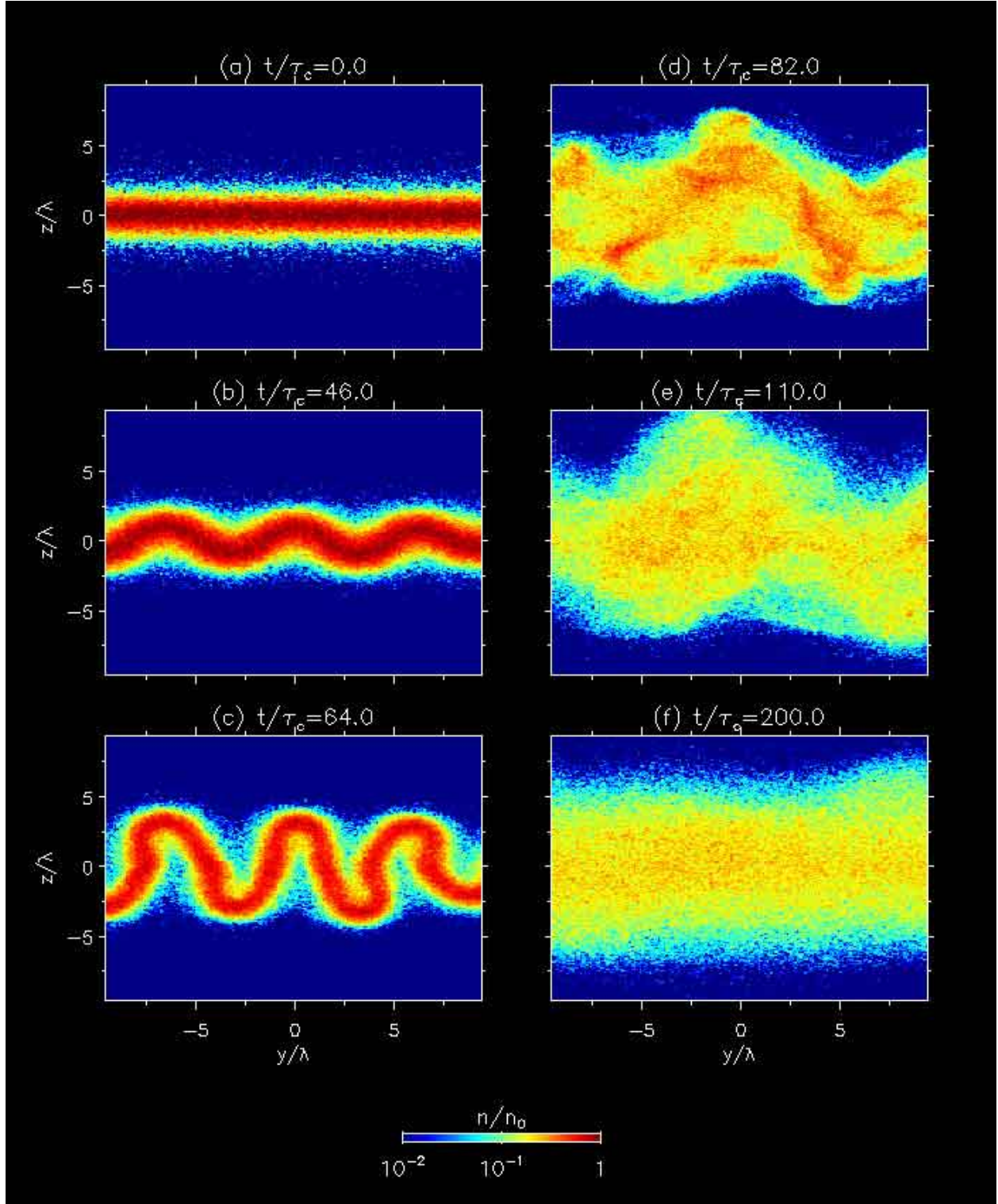


Fig. 13.— Snapshots of run D3 in the yz plane at various stages ($t/\tau_c = 0.0, 46.0, 64.0, 82.0, 110.0$, and 200.0).

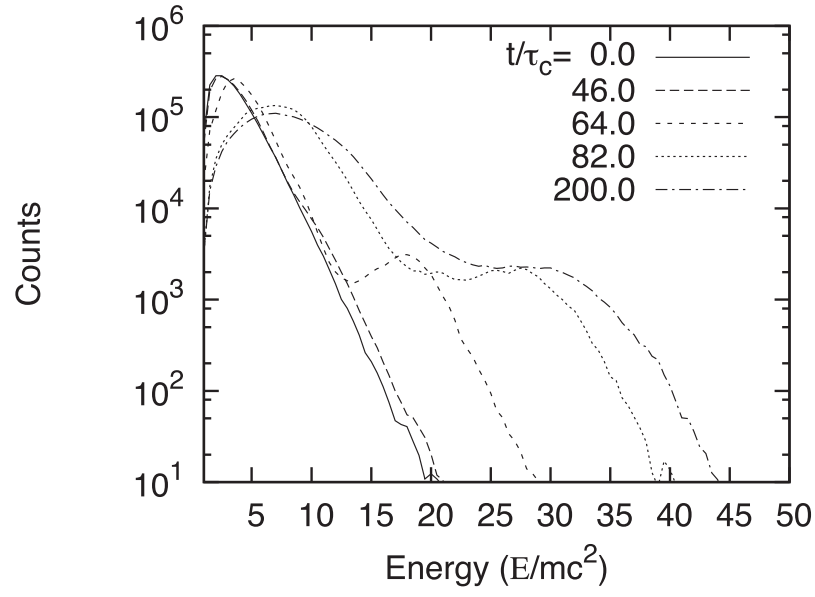


Fig. 14.— Energy spectra in run D3 at various stages. The particle count number, integrated over the main simulation box, is presented as a function of the particle energy.

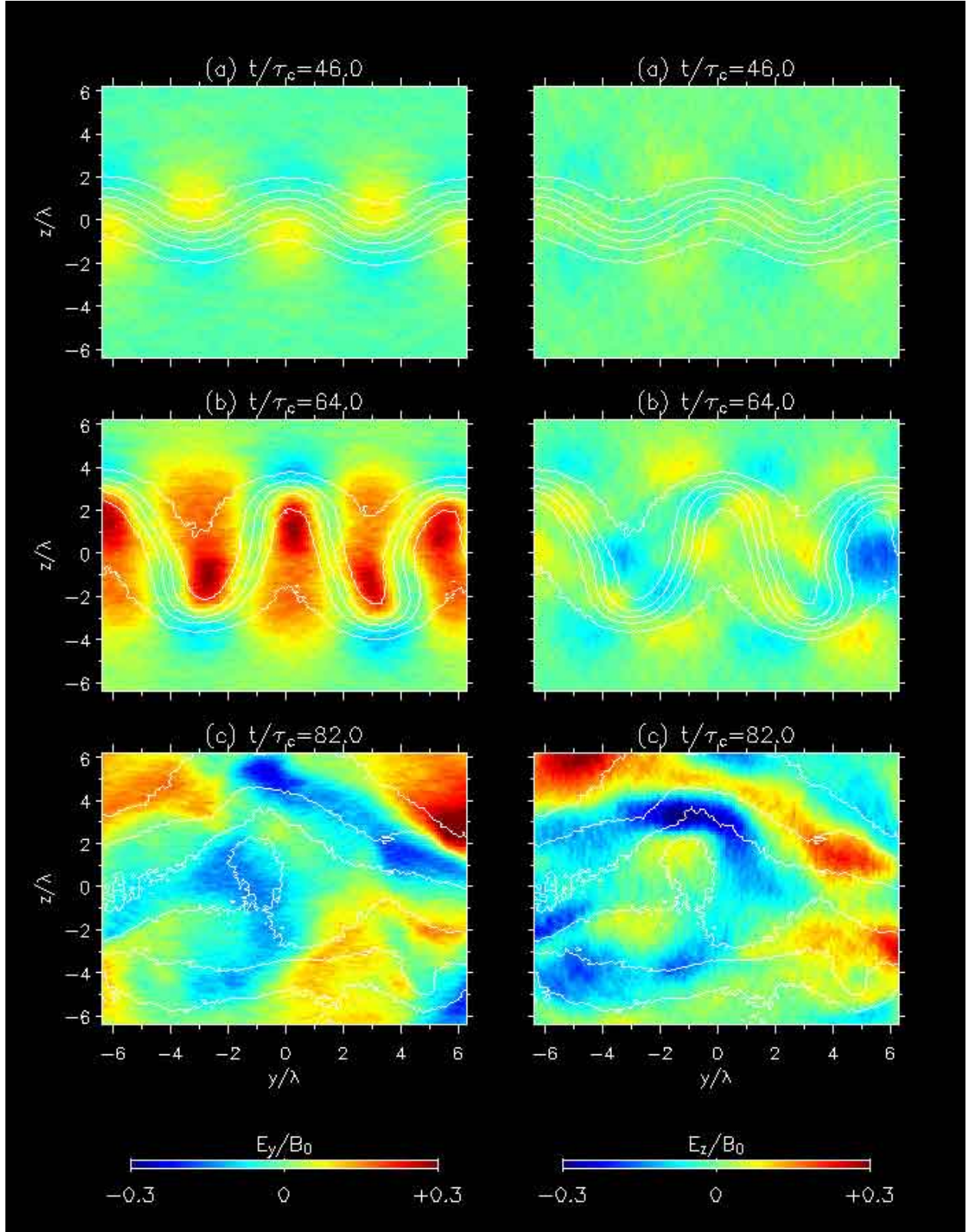


Fig. 15.— Electric fields E_y and E_z at $t/\tau_c = 46.0, 64.0$, and 82.0 . White lines show contours of B_x .

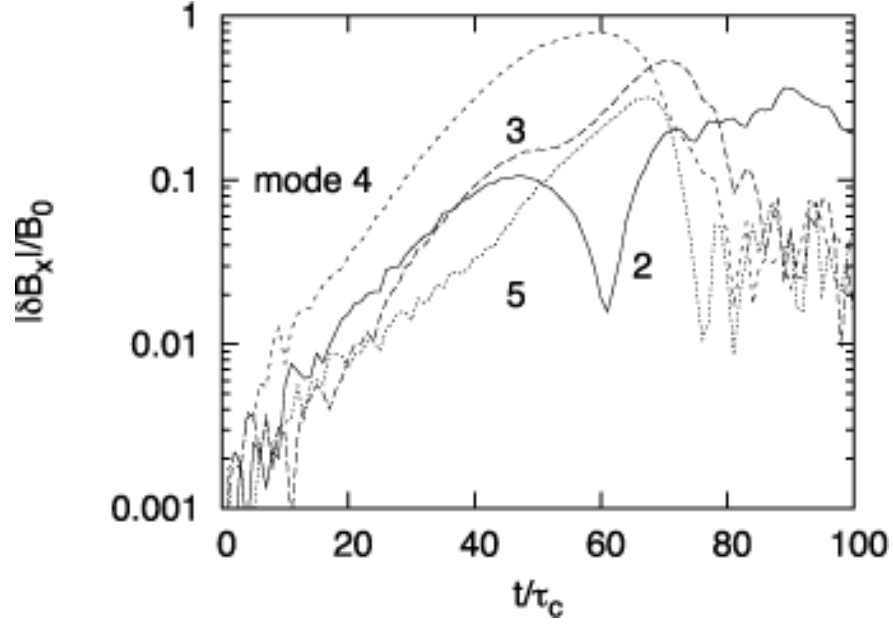


Fig. 16.— Time histories of the amplitude of perturbed magnetic field δB_x in the neutral plane ($z = 0$) for drift kink modes. Modes 2-5 correspond to $k_y \lambda = 0.49, 0.74, 0.98$, and 1.22 .

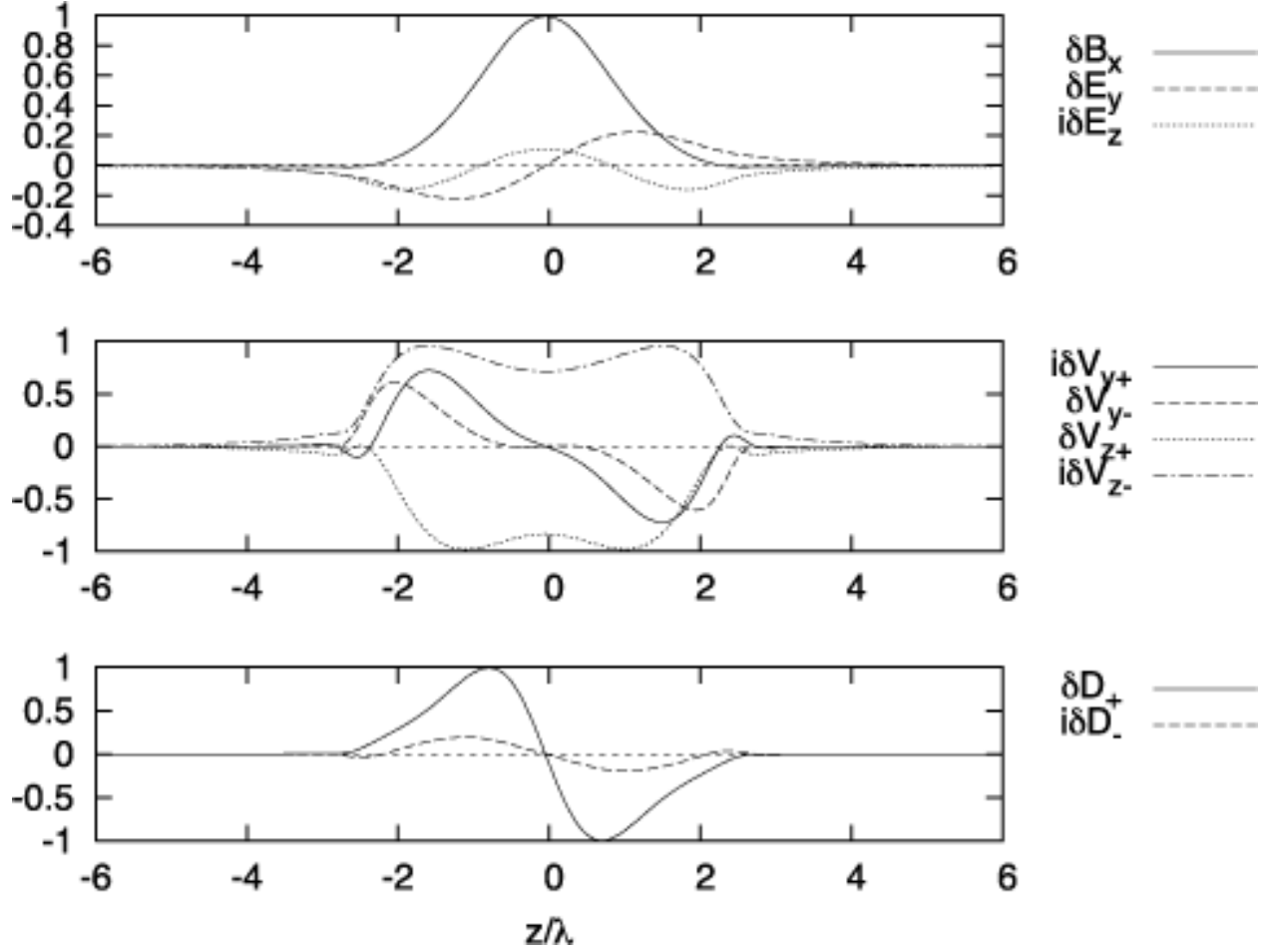


Fig. 17.— The z -profiles of the eigen functions of the relativistic drift kink instability (RDKI) for the parameter $k_y\lambda = 1.0$. *Top:* Perturbations of δB_x , δE_y and δE_z . *Middle:* Perturbed plasma velocities. The bulk velocities of plasmas are $\delta V_{\{y,z\}+} = \delta v_{\{y,z\}p} + \delta v_{\{y,z\}e}$ and the relative velocities of the two species are $\delta V_{\{y,z\}-} = \delta v_{\{y,z\}p} - \delta v_{\{y,z\}e}$. *Bottom:* The density perturbations are presented: $\delta D_+ = \delta d_p + \delta d_e$ and $\delta D_- = \delta d_p - \delta d_e$.

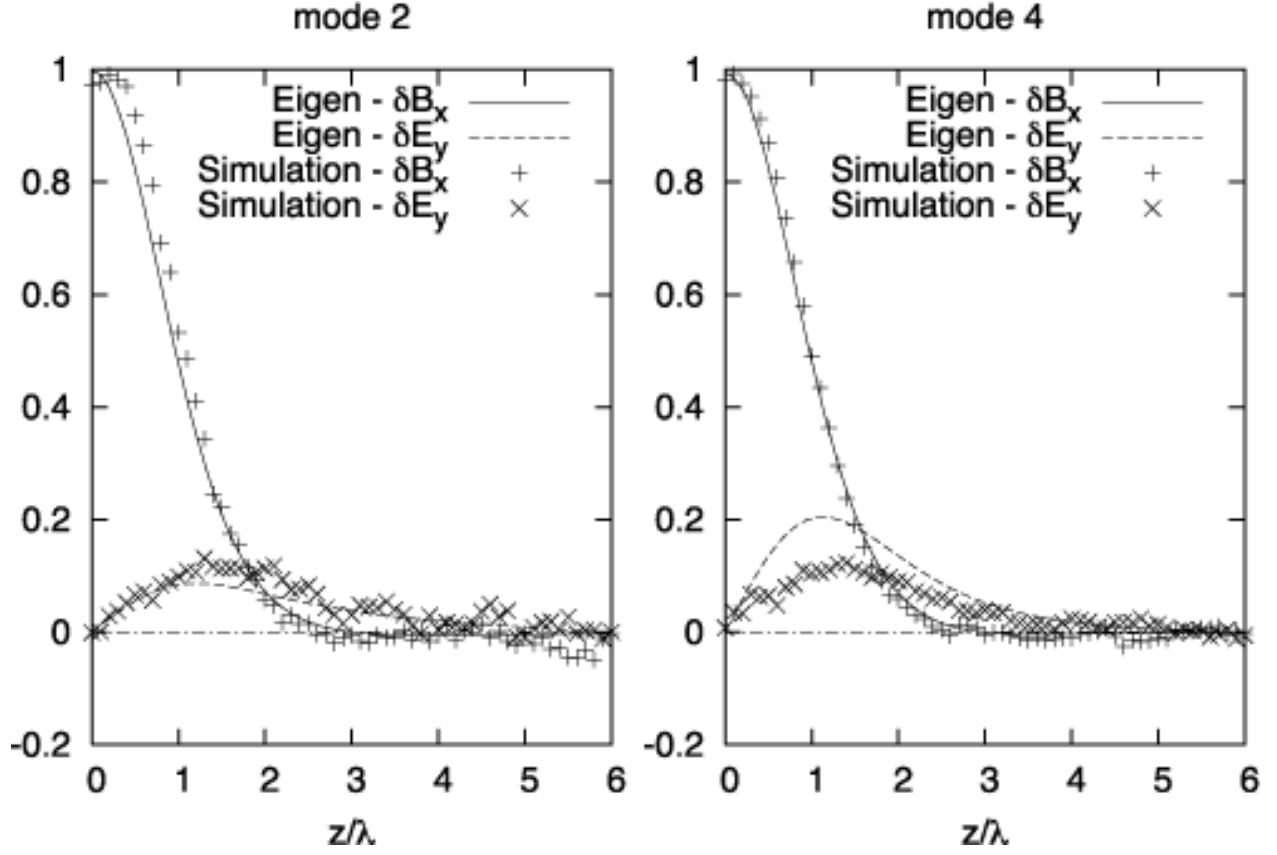


Fig. 18.— Perturbation profiles of the simulation data and relevant eigen modes. *Left*: Mode 2 ($k\lambda = 0.49$) and the eigenmode for $k\lambda = 0.50$. *Right*: Mode 4 ($k\lambda = 0.98$) and the eigenmode for $k\lambda = 1.00$.

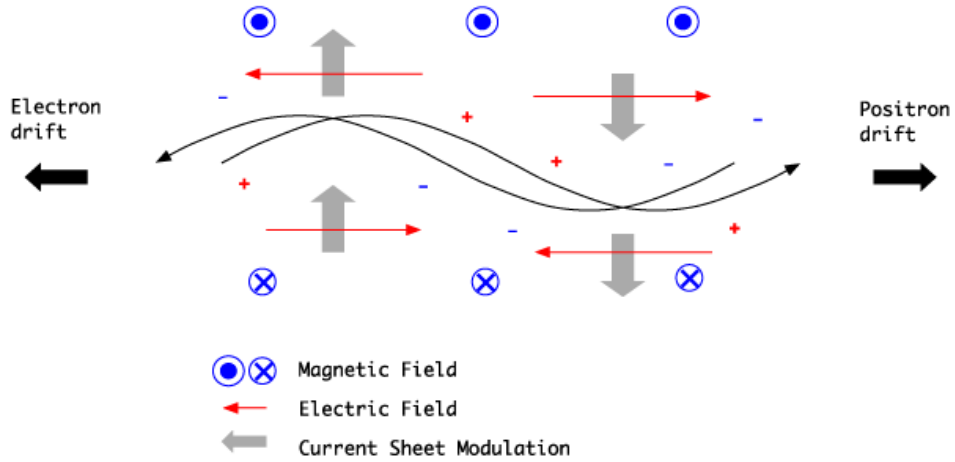


Fig. 19.— Schematic explanation of charge separation in the RDKI

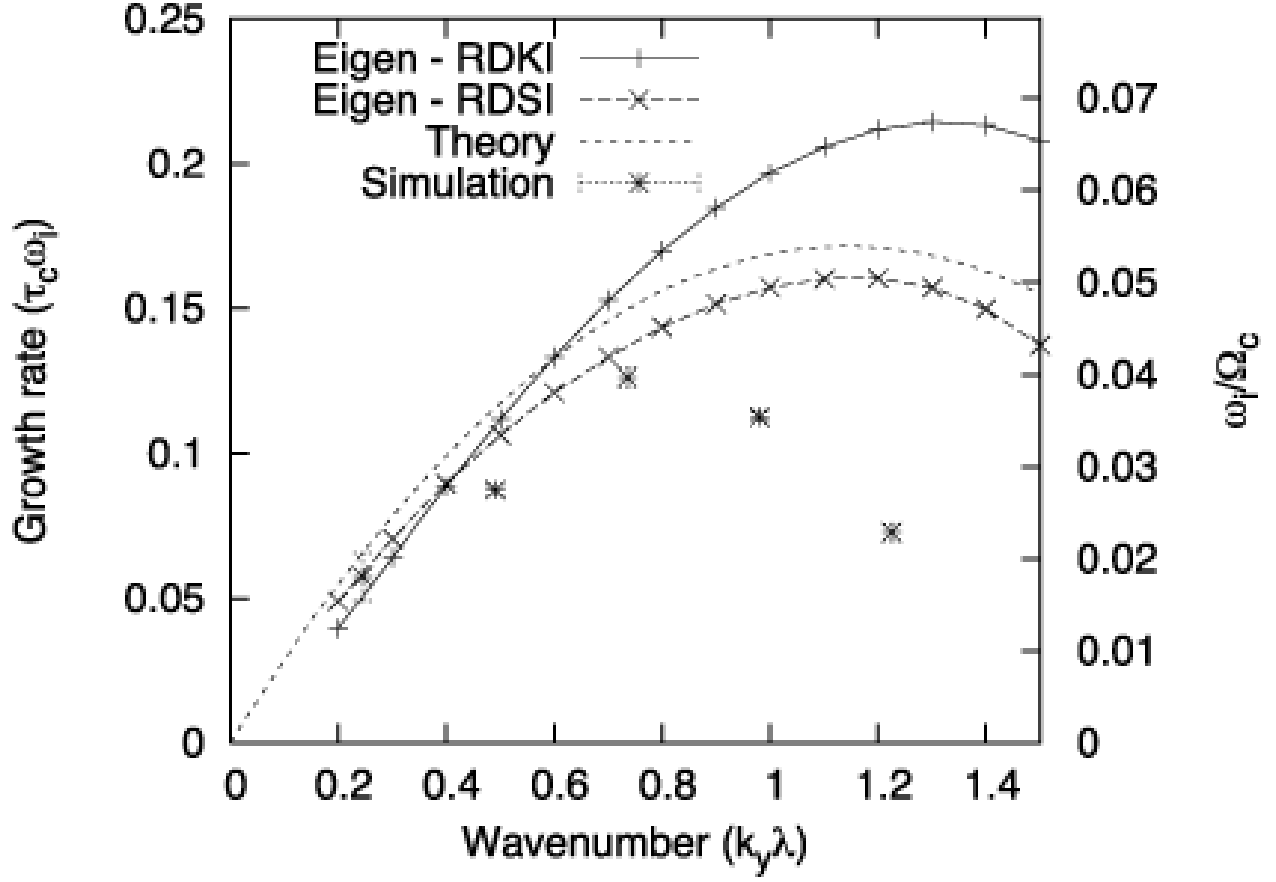


Fig. 20.— Growth rates of the RDKI (ω_i) as a function of the normalized wavenumber ($k_y \lambda$). Eigen growth rates (*solid line with plus symbols*), another branch of eigen growth rates (*dashed line with crosses*), eq. (25) (*dashed line*), and simulation results (*asterisks*). The timescale is presented in units of τ_c (*left axis*) and Ω_c (*right axis*).

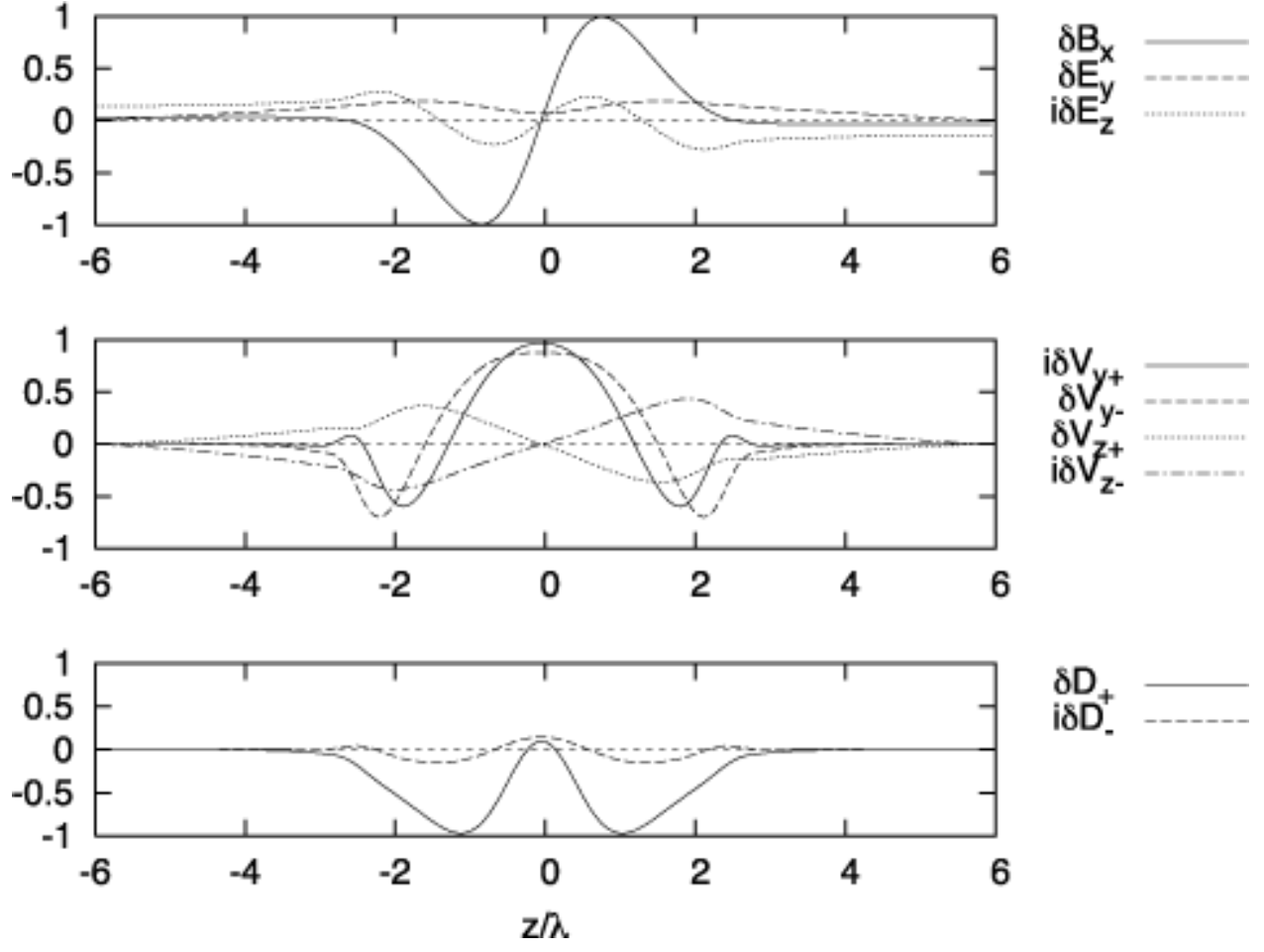


Fig. 21.— Same as Fig. 17 but for the relativistic drift sausage instability (RDSI) with the parameter $k_y\lambda = 0.25$.

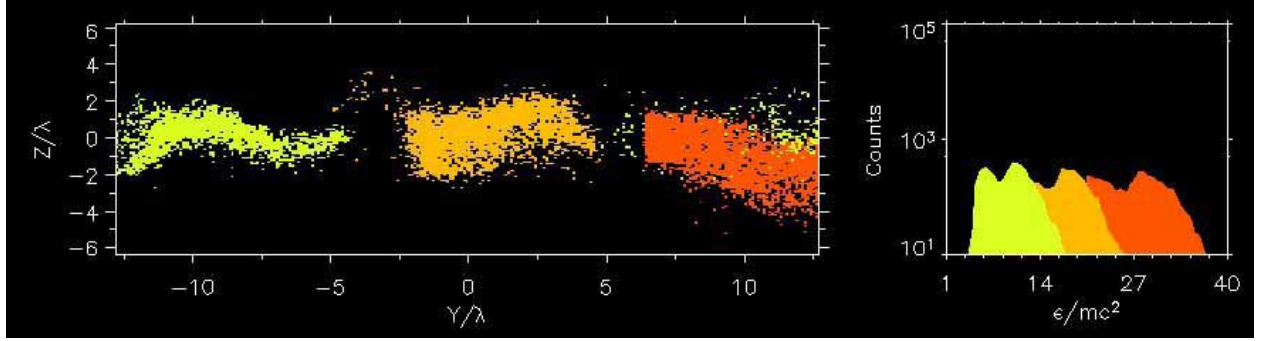


Fig. 22.— Spatial distributions and energy spectra of selected positrons, which satisfies the following two criteria: (1) the kinetic energy satisfies $\varepsilon/mc^2 > 20$ at $t/\tau_c = 82.0$ and (2) the y -position satisfies $6.4 \leq y/\lambda < 12.8$ at $t/\tau_c = 82.0$. Three stages of the distribution are presented, $t/\tau_c = 46.0$ (light gray or yellow), 64.0 (gray or light orange) and 82.0 (dark gray or deep orange).

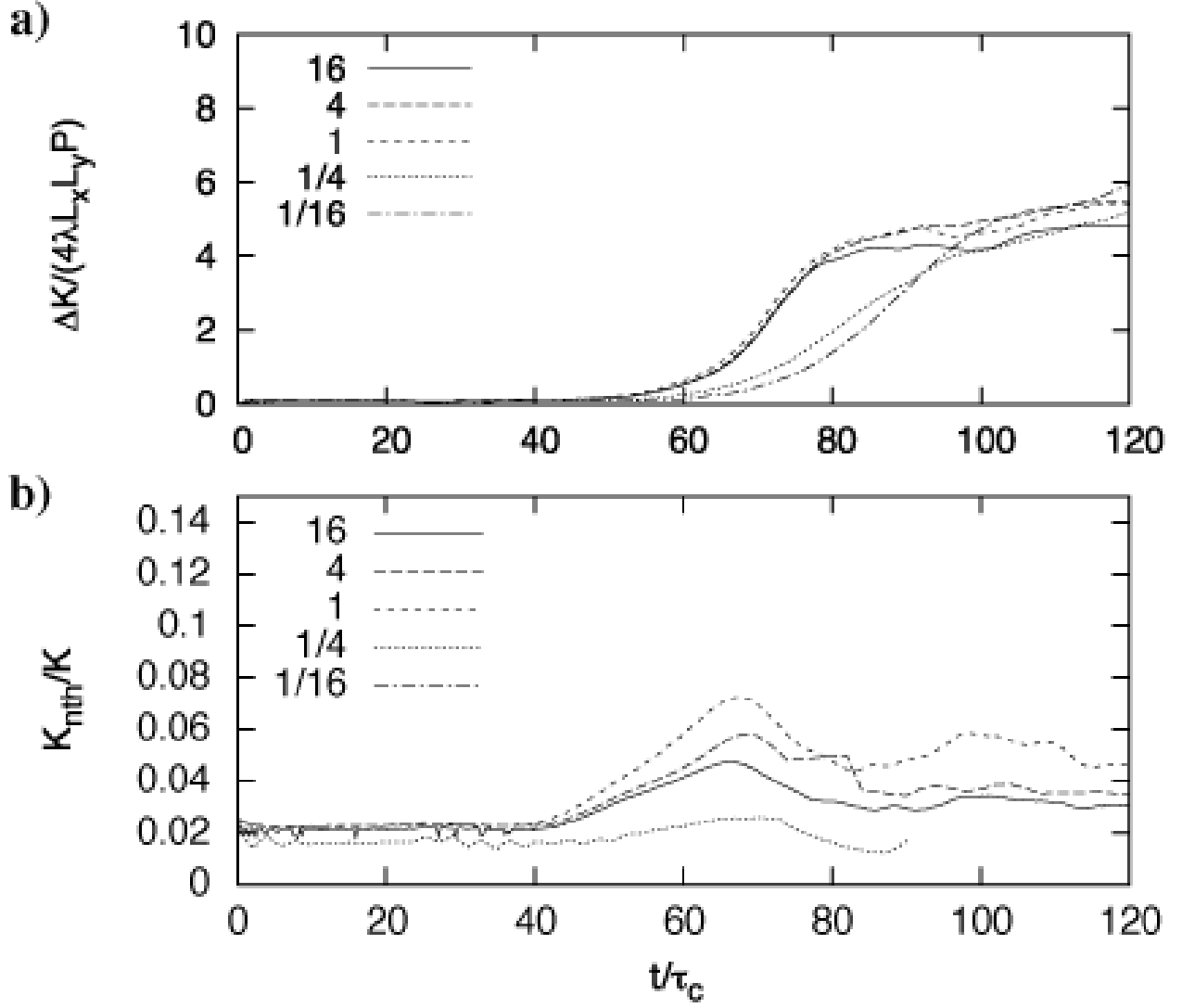


Fig. 23.— (a) Enhancements of the particle kinetic energies in the RDKI runs. Energies and time are normalized by the pressure in the original current sheet and the light transit time, respectively. (b) Ratio of nonthermal energy in the case of the RDKI runs. The ratio for $T/mc^2 = 1/16$ cannot be calculated by our method.

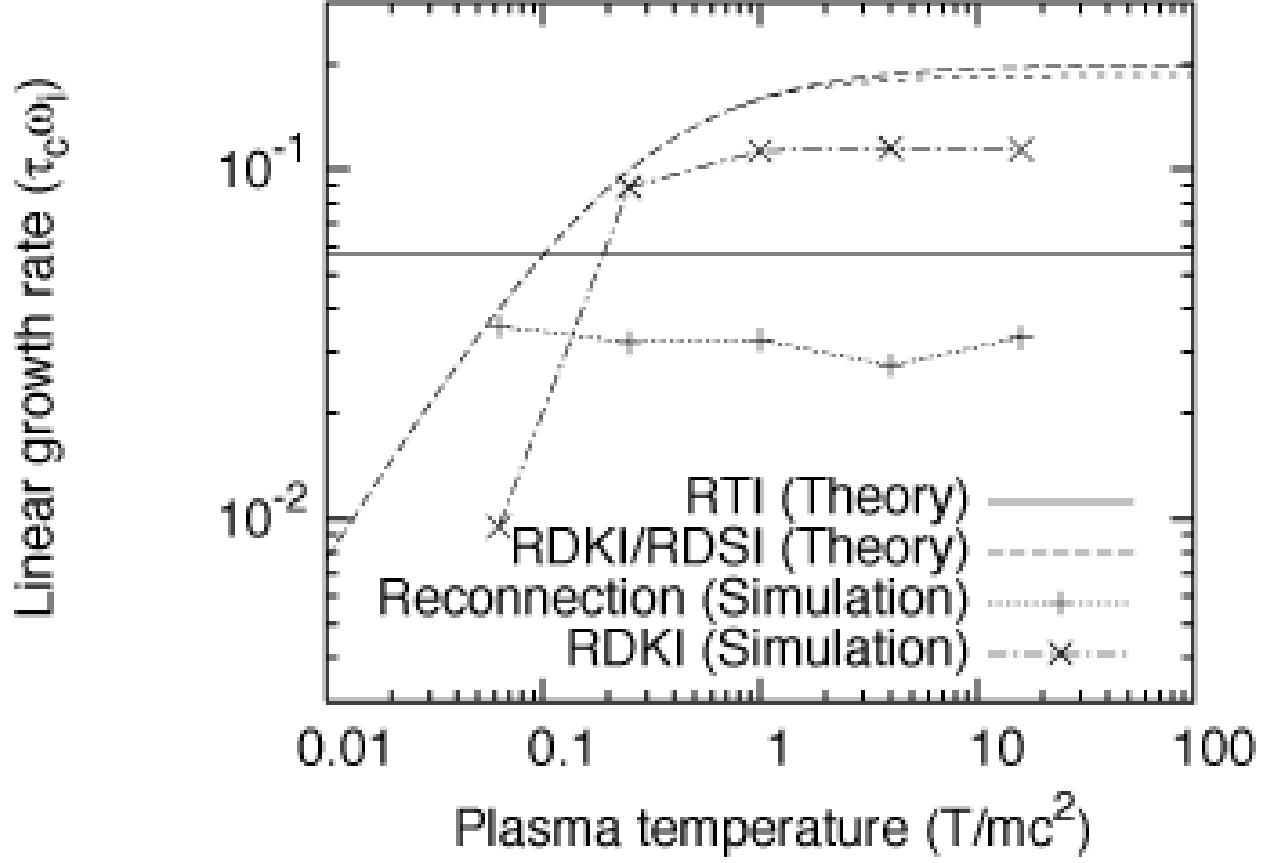


Fig. 24.— Temperature dependency of the growth rates ($\tau_c \omega_i$). Theoretical growth rates of RTI and RDKI, and observed growth rates of magnetic reconnection and the RDKI are presented.

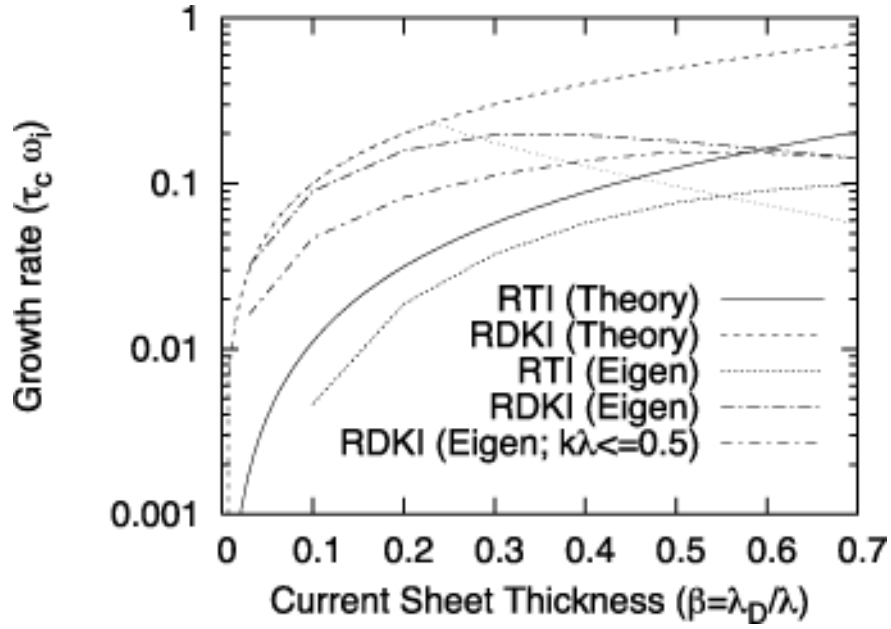


Fig. 25.— Growth rates of the instabilities as a function of the current sheet thickness $\beta = \lambda_D/\lambda$. The growth rate ω_i is presented in a timescale of τ_c . Upper limit of the RDKI β (from eq. [30]), upper limit of the relativistic tearing mode $0.35\beta^{3/2}$ (from eq. [35]), obtained eigen growth rates for the tearing mode, obtained eigen growth rates for the RDKI and eigen growth rates for the RDKI for short wavelength are shown.

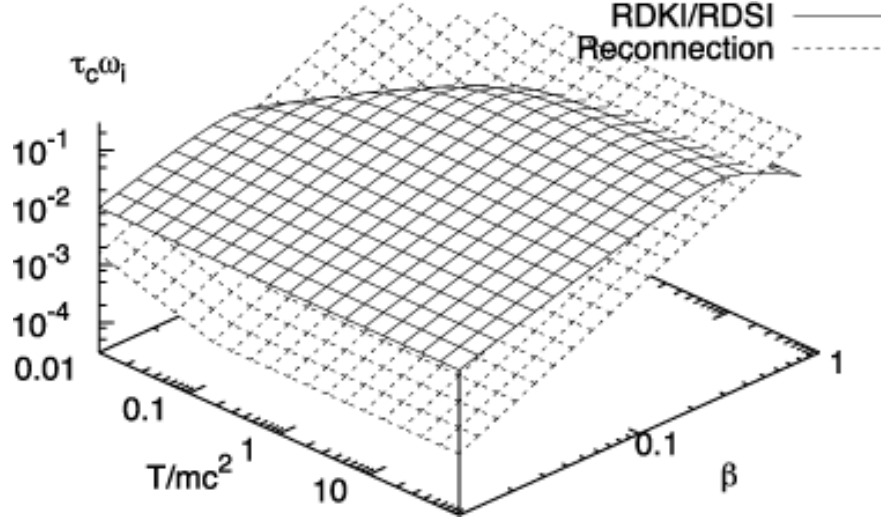


Fig. 26.— Theoretical estimate of the growth rates ω_i , as a function of the plasma temperature T/mc^2 and the drift speed β . The dashed surface shows linear growth rates of magnetic reconnection in electron-positron plasmas, based on Zelenyi & Krasnoselskikh (1979). The solid surface shows the upper limit growth rates of the drift kink/sausage instability.

Table 2. Simple estimates of KS03 scenarios

Dissipation	q	r_{max}/r_{LC}	r_{max}/r_{LC}	$\Delta(r/r_{LC})^{-q}$
Tearing-mode (modified)	5/12	$0.75 \cdot \mu^{4/5} \hat{L}^{3/10}$	9.3×10^9	$[5^8 0.35^2 / (19^7 12 \pi^2)]^{1/12} \mu^{-1/3} \hat{L}^{-1/8}$
Tearing-mode (KS03)	5/12	$0.5 \cdot \mu^{4/5} \hat{L}^{3/10}$	6.1×10^9	$[5^8 / (19^7 12 \pi^2)]^{1/12} \mu^{-1/3} \hat{L}^{-1/8}$
Drift-kink-mode	2/5	$0.25 \cdot \sqrt{\pi} \mu \hat{L}^{1/4}$	3.1×10^9	$4^{-3/5} \pi^{1/5} \mu^{-2/5} \hat{L}^{-1/10}$
Fast (KS03)	1/3	$0.1 \mu^2 (1 - \beta_c^2) / \beta_c$	4.6×10^7	$\{6 \beta_c / [25 \pi (1 - \beta_c^2)]\}^{1/3} \mu^{2/3}$

Note. — The dissipation index q , the dissipation distance r_{max} , its estimated value, and the factor for Δ are shown. The Crab parameters $\mu = 2 \times 10^4$ and $\hat{L} = 1.5 \times 10^{22}$ are the total energy carried by the wind per unit rest mass (eq. [23] in KS03) and the dimensionless flow luminosity (eq. [29] in KS03), respectively.

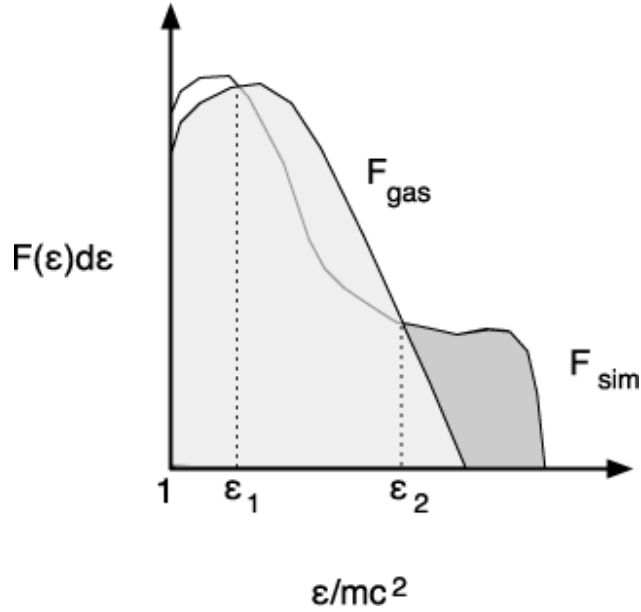


Fig. 27.— Relation between the observed distribution F_{sim} (white and dark gray) and the equivalent thermal distribution F_{gas} (light gray). Two parameters ε_1 and ε_2 represent crossing points of the two spectra. The high-energy tail region in dark gray carries the “nonthermal” energy.

Table 3. List of simulation runs

Run	T/mc^2	L_x	L_y	L_z	c/ω_c	c/ω_p	$\frac{n_{bg}}{(\gamma\beta n_0)}$	n_{total}	K_{nth}/K	$\tau_c\omega_i$	ε_{max}/mc^2	ε_{est}/mc^2
R1	16	102.4	–	51.2	0.01	0.077	5%	1.7×10^7	$> 3.5 \times 10^{-1}$	3.3×10^{-2}	$> 3.4 \times 10^3$	5.6×10^3
R2	4	102.4	–	51.2	0.04	0.15	5%	1.7×10^7	$> 3.7 \times 10^{-1}$	2.8×10^{-2}	$> 6.9 \times 10^2$	1.4×10^3
R3	1	102.4	–	51.2	0.16	0.31	5%	1.7×10^7	$> 3.7 \times 10^{-1}$	3.3×10^{-2}	$> 1.5 \times 10^2$	3.5×10^2
R4	1/4	102.4	–	51.2	0.63	0.61	5%	1.7×10^7	$> 3.4 \times 10^{-1}$	3.2×10^{-2}	$> 4.0 \times 10^1$	8.7×10^1
R5	1/16	102.4	–	51.2	2.5	1.2	5%	1.7×10^7	$> 1.1 \times 10^{-1}$	3.6×10^{-2}	$> 1.1 \times 10^1$	2.2×10^1
D1	16	–	25.6	51.2	0.01	0.077	0	4.2×10^6	4.7×10^{-2}	1.1×10^{-1}	7.0×10^2	7.1×10^2
D2	4	–	25.6	51.2	0.04	0.15	0	4.2×10^6	5.8×10^{-2}	1.2×10^{-1}	1.9×10^2	1.6×10^2
D3	1	–	25.6	51.2	0.16	0.31	0	4.2×10^6	7.2×10^{-2}	1.1×10^{-1}	4.8×10^1	4.2×10^1
D4	1/4	–	25.6	51.2	0.63	0.61	0	4.2×10^6	2.6×10^{-2}	8.9×10^{-2}	10.0	9.9
D5	1/16	–	25.6	51.2	2.5	1.2	0	4.2×10^6	N/A	9.5×10^{-3}	4.0	3.0
R0	$\sim 1/4$	102.4	–	51.2	0.54	0.54	1%	6.7×10^7	–	–	–	–
D3a	1	–	25.6	51.2	0.16	0.31	5%	4.2×10^6	3.0×10^{-2}	1.1×10^{-1}	4.5×10^1	4.2×10^1
D3b	1	–	25.6	38.4	0.16	0.31	0	4.2×10^6	–	–	–	–
D3c	1	–	25.6	25.6	0.16	0.31	0	2.1×10^6	–	–	–	–

Note. — Initial parameters and obtained physical values of simulation runs in this paper. Runs R0 and R1-R5 are for magnetic reconnection. Runs D1-D5, D3a-D3c are for the DKI. The temperature (T/mc^2), the system size (L_x, L_y, L_z in units of λ), the unit gyroradius (in units of λ), the unit inertial length (in units of λ), the ratio of the background plasma density (n_{bg}) to the plasma density in the current sheet ($\gamma\beta n_0$), the total number of the particles (n_{total}), the nonthermal ratio (K_{nth}/K), the linear growth rate ($\tau_c\omega_i$), the maximum energy (ε_{max}/mc^2), and their estimated values (ε_{est}/mc^2) are listed.